

Laminar and transitional liquid metal duct flow near a magnetic point dipole

S. Typel, T. Boeck and J. Schumacher

Institut für Thermo- und Fluidodynamik, Technische Universität Ilmenau, Postfach 100565, D-98684 Ilmenau, Germany

(Dated: April 4, 2024)

The flow transformation and the generation of vortex structures by a strong magnetic dipole field in a liquid metal duct flow is studied by means of three-dimensional direct numerical simulations. The dipole is considered as the paradigm for a magnetic obstacle which will deviate the streamlines due to Lorentz forces acting on the fluid elements. The duct is of square cross-section. The dipole is located above the top wall and is centered in spanwise direction. Our model uses the quasi-static approximation which is applicable in the limit of small magnetic Reynolds numbers. The analysis covers the stationary flow regime at small hydrodynamic Reynolds numbers Re as well as the transitional time-dependent regime at higher values which may generate a turbulent flow in the wake of the magnetic obstacle. We present a systematic study of these two basic flow regimes and their dependence on Re and on the Hartmann number Ha , a measure of the strength of the magnetic dipole field. Furthermore, three orientations of the dipole are compared: streamwise, spanwise and wall-normal oriented dipole axes. The most efficient generation of turbulence at a fixed distance above the duct follows for the spanwise orientation, which is caused by a certain configuration of Hartmann layers and reversed flow at the top plate. The enstrophy in the turbulent wake grows linearly with Ha which is connected with a dominance of the wall-normal derivative of the streamwise velocity.

PACS numbers: 47.35.Tv, 47.65.-d

I. INTRODUCTION

Fluid motion which is interacting with electromagnetic fields plays a central role for the dynamics in the interior and atmospheres of stars^{9,47} or in nuclear fusion⁴³. Although less spectacular, such interactions also occur in flows of molten metals in technological applications ranging from the generation of monocrystals for silicon wafers to the production of steel and complex alloys for industrial manufacturing¹⁴. Understanding the basic mechanisms of how an electromagnetic field generates or suppresses fluid motion is a prerequisite for the efficient electromagnetic control of such technological processes. Applying this knowledge may for example improve the purity of the materials.

Apart from flow control, electromagnetic fields can also be employed for flow measurement in conducting liquids. Inductive flow meters determine the fluid velocity from the voltage induced across the flow as it traverses a magnetic field⁴⁹. This method is well-established and very accurate. However, it is not contactless but requires electrodes in the liquid. It is therefore not suited for hot and aggressive molten metals. Several efforts of the last decade have, therefore, been devoted to the development of contact-less methods for such non-transparent liquids based on electromagnetic induction. Examples of such methods are the contactless inductive flow tomography⁵², the rotary flow meter⁴⁶ and Lorentz Force Velocimetry (LFV)^{53,54}.

In LFV, the currents which are induced in the flow by an external magnet system result in a braking force on the flow. Conversely, the flow exerts a reaction force on the magnet on account of Newton's third law. This Lorentz force on the magnet depends on the velocity magnitude and distribution, and can be used for velocity measurement. The state of the art in LFV is largely limited to global measurements, i. e., mean velocities or volume fluxes of the liquid metal flow. The utility of LFV for local measurement has been demonstrated only very recently for the wake behind a solid obstacle²³. It requires a localized field that pervades only a small portion of the flow domain, where the flow can be significantly modified by the Lorentz force. Further development of LFV for detailed, spatially resolved measurements requires a better understanding of such aspects. They have to be studied by direct numerical simulations (DNS) since only DNS can provide the fully resolved space-time evolution of three-dimensional liquid metal flows and Lorentz force components that affect the motion. By means of DNS, the *local impact* of the magnetic field and the related parameter dependencies can be studied systematically in laminar, transient or turbulent cases. Because of the high computational cost of DNS, this approach will remain limited to a moderate range of dimensionless parameters, i. e., Reynolds and Hartmann numbers, Re and Ha .

In recent years, computations of liquid-metal magnetohydrodynamic (MHD) flows have become more frequent, and a number of DNS studies have been reported. Typically, such works were concerned with effects arising from the anisotropic nature of the Joule damping and from the specific MHD boundary layers at walls^{10,11,30,33,34,58,62}. Instabilities of MHD boundary layers such as the Hartmann layer, and the transition to turbulence have been analyzed numerically in ducts and channels for homogeneous magnetic fields^{2,19,31,35,36,48}. From the LFV perspective, such investigations are of limited interest because the total Lorentz force vanishes in the case of a homogeneous field.

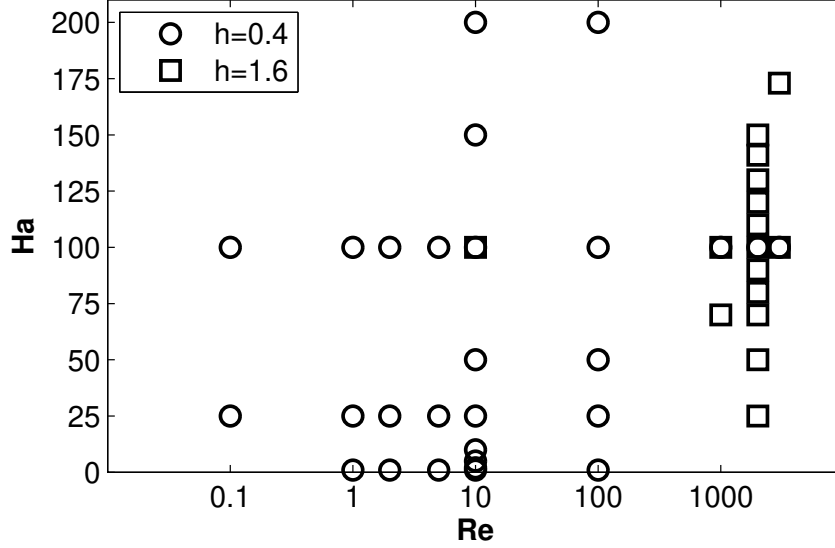


FIG. 1: Parameter sets of Hartmann and Reynolds numbers, Ha and Re investigated. Each point denotes a separate direct numerical simulation. The distances h of the dipole from the top surface of the duct is $h = 0.4$ (circles) or $h = 1.6$ (squares) measured in units of the half width of the duct.

The aim of this article is to investigate the structure formation and the locally resolved Lorentz force fields in a liquid metal duct flow in the presence of a magnetic point dipole field. The flow and magnetic field configurations are similar to recent laboratory experiments on LFV using liquid InGaSn alloy at room temperature²⁴. We conduct three-dimensional DNS based on the quasi-static approximation of the induction equation. This approximation applies for liquid metal flows with a high conductivity which are considered here and can be found typically in laboratory experiments and industrial applications¹⁶. The induced magnetic field is then weak and does not modify the stronger primary magnetic field significantly. Hence, the induced currents depend linearly on the velocity field and can be computed from Ohm's law for a moving conductor with the electric field represented by a potential gradient.

In terms of the flow geometry, we will focus on a straight duct flow with square cross section as one of the simplest shear flow configurations. Our choice of a magnetic dipole field is also guided by mathematical simplicity and by its rapid decay. A drawback is that it represents the far field of a typical permanent magnet, i.e., it will not provide a very good approximation when such a magnet is placed close to the duct²⁴. Because of the rapid decay, the magnetohydrodynamic interaction of the dipole field with the flow is strongly localized and three-dimensional. We will demonstrate that it can cause a locally pronounced deflection of the velocity field for laminar flows, and that the wake of the dipole is characterized by vortical structures at higher velocities. For particular orientations of the magnetic dipole moment, transition to turbulence in the wake is observed at moderate Reynolds numbers. In order to keep the parameter space manageable we only consider three basic orientations of the magnetic dipole moment, namely along the streamwise, spanwise and wall-normal directions.

The present study can be regarded as a continuation of the theoretical and numerical investigations reported in²⁴. In this previous work, dynamic effects of the Lorentz force on the flow were only significant in the creeping flow regime. As before, we shall not only consider the flow modification but also determine the electromagnetic force and torque on the dipole, which are of great interest from the perspective of LFV.

Without reference to LFV, the flow modification by a localized magnetic field has also been investigated by other authors.¹² have termed it magnetic obstacle in analogy with the flow around a solid obstacle. Similar configurations have been investigated both experimentally and numerically^{6,7,29,59,60}. The magnetic fields in these works typically had a lower degree of spatial non-uniformity, and cannot be characterized in such a simple way as a point dipole. A point dipole has been used for analytic investigations in Cuevas et al. (2006)¹³, but for a quasi two-dimensional problem. In addition, force and torque on the magnet system were typically also not studied, and three-dimensional simulations were performed with relatively coarse grids (e.g. Votyakov et al. (2008)⁶⁰). We therefore also attempt to significantly improve on these earlier works in terms of numerical resolution.

Naturally, the geometric parameters such as position and orientation of the magnetic dipole, have a strong influence on the acting forces. However, a detailed investigation of this point would go beyond the scope of this article. Indeed, we will focus on the influence of the hydrodynamic Reynolds number Re and the Hartmann number Ha . In brief, the

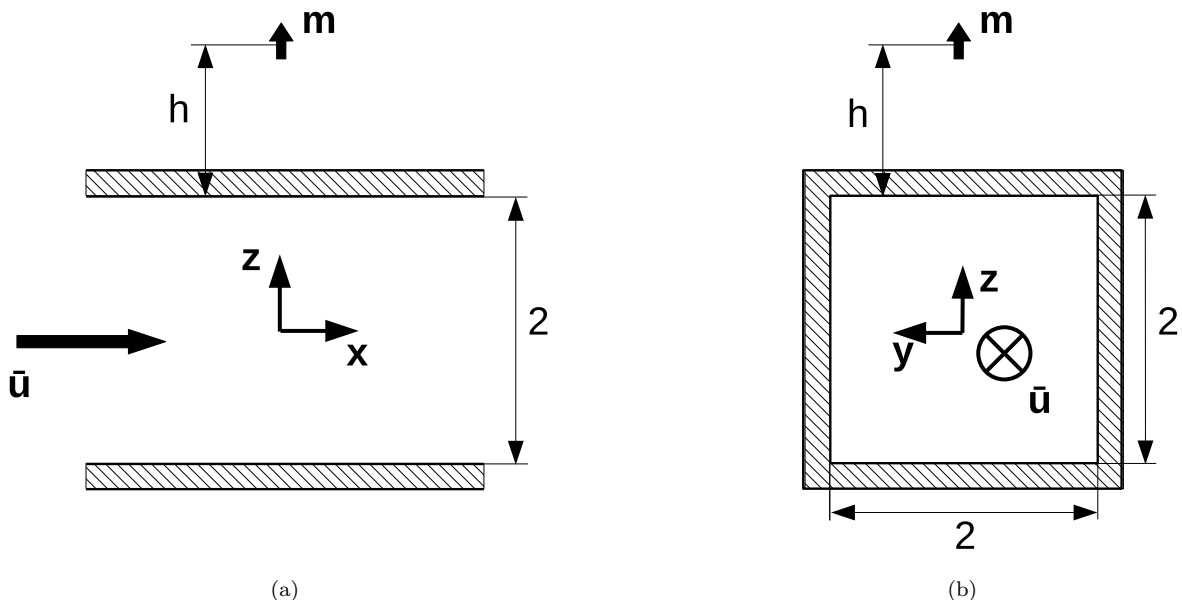


FIG. 2: Setup of the problem. (a) Side view. (b) Rear view. – The mean velocity \bar{u} of the duct flow points in positive x -direction. The origin of the coordinate system is placed at the center of the duct. The distance between magnetic point dipole and fluid surface is denoted as h . The characteristic length scale of this setup is chosen to be the half-width of the duct. All lengths are expressed in this unit.

Reynolds number describes the ratio of the inertial to the viscous forces in the flow (mathematical definitions of both numbers will be given in Eqns. (4) and (5)). The Hartmann number is a measure for the strength of the magnetic field and its influence on the flow. Both parameters are investigated in a wide range, as displayed in Fig. 1. Since it is understood that the position of the dipole is important for the spatial development and transformation of the flow, we consider two particular distances between dipole and duct. In particular, a very short distance is used for the lower Reynolds numbers, as this allows a direct comparison with recent laboratory experiments by Heinicke et al. (20012)²⁴. At higher Reynolds numbers the magnetic dipole is positioned further away from the top wall of the duct. This changes the magnetic field configuration inside the flow and excites vortices that will eventually cause the flow to become turbulent.

The article is organized as follows. First, we introduce the geometry and setting of the problem under consideration in Sec. II A and explain the numerical method in Sec. II B. Second, we present the results for low Reynolds number to describe the basic deformations of the flow field in Sec. III in the stationary regime. This regime exists for the lower Reynolds numbers and persists when both, Ha and Re , are increased to a certain point. In Sec. IV, we discuss the transition to turbulence when the Reynolds number is further increased. Conclusions and a brief outlook are given in Sec. V.

II. DEFINITION OF THE PROBLEM

A. Equations of motion and setup

We consider the flow of an electrically conducting fluid in a square duct of side length $2L$, i.e., the characteristic length L will be defined as the half width of the duct. We use Cartesian coordinates, where the streamwise direction is denoted as x , the spanwise direction as y and the vertical, wall-normal direction as z . The duct is exposed to the inhomogeneous magnetic field of a point dipole located at a vertical distance H above the top surface of the duct. In dimensional units, the dipole field at position \vec{x} is given by²⁶

$$\vec{B} = \frac{\mu_0 M}{4\pi} \left(\frac{3\vec{m} \cdot \vec{r}}{|\vec{r}|^5} \vec{r} - \frac{\vec{m}}{|\vec{r}|^3} \right), \quad (1)$$

where M denotes the magnetic dipole moment and the unit vector \vec{m} its orientation. The other quantities are the vacuum permeability μ_0 and the distance $\vec{r} = \vec{x} - \vec{r}_0$ between \vec{x} and the dipole position at \vec{r}_0 . For nondimensionalization of the problem we use the maximum value

$$B_{max} = \frac{\mu_0 M}{4\pi H^3} \sqrt{m_x^2 + m_y^2 + 4m_z^2} \quad (2)$$

of the dipole field within the duct as unit of magnetic induction.

Based on B_{max} and L as unit of length, the nondimensional magnetic flux density of the dipole is

$$\vec{B}'(\vec{x}') = \frac{h^3}{\sqrt{m_x^2 + m_y^2 + 4m_z^2}} \left(\frac{3\vec{m} \cdot \vec{r}'}{|\vec{r}'|^5} \vec{r}' - \frac{\vec{m}}{|\vec{r}'|^3} \right), \quad (3)$$

where $h = H/L$ is the nondimensional distance between dipole and duct and nondimensional quantities are indicated by a prime. In the following, we shall use nondimensional quantities exclusively and will therefore omit the prime in subsequent equations.

A sketch of the setup in dimensionless units is shown in Fig. 2. The origin is chosen to be at the centerline of the duct. Thus the duct extends in y and z -direction from -1 to 1. The position of the dipole is given by $\vec{r}_0 = (0, 0, h + 1)$, i. e., in the vertical center plane. A key parameter of our study is the orientation of the magnetic moment of the point dipole, which is referred to as the dipole orientation. We will call the orientation streamwise if $\vec{m} = \vec{e}_x$, spanwise if $\vec{m} = \vec{e}_y$ and vertical if $\vec{m} = \vec{e}_z$. In this article, we only consider these three main orientations, but preliminary studies have shown that oblique orientations lead to more complex structures in the flow which will be discussed elsewhere.

As mentioned above, the dipole field approximates the far field of a small permanent magnet. Close to the permanent magnet the dipole is not a very accurate model for the actual field. Nevertheless, the differences are not substantial. We have measured the field distribution around a cube magnet of 1 cm side length and compared it with a point dipole. The dipole moment was chosen such that the magnetic induction agrees between the cube magnet and the dipole at 1 cm distance from its center. The magnetic induction was compared along the dipole axis for distances greater than 1 cm. At identical positions, the relative error in magnetic induction between dipole and cube magnet never exceeded 30%. Details can be found in Tynpel (2013)⁵⁵.

Before listing the equations that will be solved numerically, we want to recall the basic physical principle which causes the deflection of the fluid motion. Inside the square duct, there is a laminar pressure-driven flow of an electrically conducting liquid. The magnetic dipole close to the duct induces electric currents, which are confined to the flow due to the insulating walls. These currents give rise to two effects. First, they induce a secondary magnetic field. This secondary magnetic field will be much weaker than the primary field of the point dipole. In many applications in metallurgy, one may assume that the secondary magnetic field is negligible. This idea coincides with the assumption that the *magnetic* Reynolds number $Rm^{16,39}$ is very small. Therefore, we can neglect the secondary field and apply the quasistatic approximation. Physically, this means that the flow is unable to deform the field lines of the magnetic dipole. There is no feedback from the flow onto the magnetic field.

Second, the currents induced by the primary magnetic field of the dipole generate a Lorentz force within the liquid. It gives rise to a strong deformation of the velocity profiles (cf. Sec. III) and even triggers a transition to turbulence (cf. Sec. IV). Due to Newton's third law, a counter force acts on the magnetic dipole which is of same magnitude, but of opposite sign as the total force \vec{F} on the liquid. Recent works by Heinicke et al. (2012)²⁴ were focused on the determination of this force and the derivation of mean flow properties from its magnitude. Here, we will focus on the particular impact of the Lorentz force on the local velocity field and the resulting flow transformation.

In addition to the geometry parameters, the problem depends on two dimensionless parameters Re and Ha . The Reynolds number Re is defined as

$$Re \equiv \frac{\bar{u}L}{\nu}, \quad (4)$$

where \bar{u} is a mean streamwise velocity and ν the kinematic viscosity. The strength of the magnetic field is quantified by the Hartmann number

$$Ha \equiv B_{max}L\sqrt{\frac{\sigma}{\rho\nu}}, \quad (5)$$

where ρ is the mass density and σ the electric conductivity. In contrast to the case of a uniform magnetic field, the definition of Ha in the present case is ambiguous because of the non-uniform magnetic flux density. We choose the maximum of the magnetic flux density B_{max} inside the duct. It occurs at the upper boundary of the duct right below the dipole at point $x = y = 0$ and $z = 1$.

The governing equations of the problem will be given in nondimensional form below. We use \bar{u} as unit of velocity and L as unit of length. The pressure, electric current and potential are given in units of $\rho\bar{u}^2$, $\sigma\bar{u}B_{max}$ and $\bar{u}B_{max}L$, respectively. To model the interaction between the Lorentz force \vec{f} and the conducting liquid, we solve the incompressible Navier-Stokes equations

$$\partial_t \vec{u} + (\vec{u} \cdot \nabla) \vec{u} = -\nabla p + \frac{1}{Re} \nabla^2 \vec{u} + \vec{f}, \quad (6)$$

$$\vec{f} = \frac{Ha^2}{Re} \vec{j} \times \vec{B}, \quad (7)$$

$$\nabla \cdot \vec{u} = 0. \quad (8)$$

The induced currents are given by Ohm's law

$$\vec{j} = -\nabla \phi + \vec{u} \times \vec{B}, \quad (9)$$

where the electric field is represented by the negative gradient of the electric potential ϕ . It is determined by the condition $\nabla \cdot \vec{j} = 0$, which corresponds to the Poisson equation

$$\Delta \phi = \nabla \cdot (\vec{u} \times \vec{B}). \quad (10)$$

Equations (9) and (10) constitute the quasi-static approximation¹⁶ with an imposed field \vec{B} . For the velocity, we use no-slip boundary conditions, i. e.,

$$\vec{u} = 0 \quad (11)$$

at all walls. Furthermore, all walls are insulating with zero wall-normal currents, and we therefore apply

$$\frac{\partial \phi}{\partial \vec{n}} = 0, \quad (12)$$

where \vec{n} denotes the corresponding normal direction perpendicular to the walls. In the streamwise direction, we apply periodic boundary condition in our simulations. For higher Reynolds numbers, we model in- and outflow conditions with the help of the so-called fringe force as described below in Sec. II B.

B. Numerical method using a fringe force

Our DNS are performed using the code from³². The equations of motion are discretized on a structured mesh by an explicit second-order finite-difference scheme with a collocated grid arrangement. The incompressibility constraint is satisfied by a standard projection method. The formulations proposed by⁴⁰ and⁴² are incorporated into the code making the present numerical scheme conservative for mass, momentum and electric charge. We use a hyperbolic-tangent based stretching to refine the grid in the boundary layers, i. e., the grid is non-uniform in the spanwise y - and wall-normal z -directions. In particular, the stretching function is given by³²

$$y = \frac{\tanh(\alpha_y \eta)}{\tanh(\alpha_y)} \quad (13)$$

where η is the coordinate on a uniform grid, y denotes the transformed coordinate, while α_y is the stretching coefficient. Equivalent stretching is applied in the z -direction. In the streamwise x -direction, we use periodic boundary conditions and a uniform grid spacing, and can thus apply fast Fourier transformations (FFT). This allows us to solve the Poisson equations for the pressure and the electric potential with the 2D-Poisson solver FishPack⁽¹⁾. Verifications of the code versus a spectral code and more details on the algorithm can be found in³².

The periodic streamwise boundary conditions simplify the solution of the Poisson equation. FishPack is comparatively fast and uses a direct method. The resulting drawback is to ensure that a laminar unperturbed duct flow profile is maintained upstream of the magnetic dipole. Thus, the computational domain has to be increased with increasing Reynolds number when the flow is below the threshold to transition to turbulence. In case of low Reynolds numbers, $Re \lesssim 10$, a periodicity length of 5π was sufficient for the laminar duct profile to be completely reestablished at the

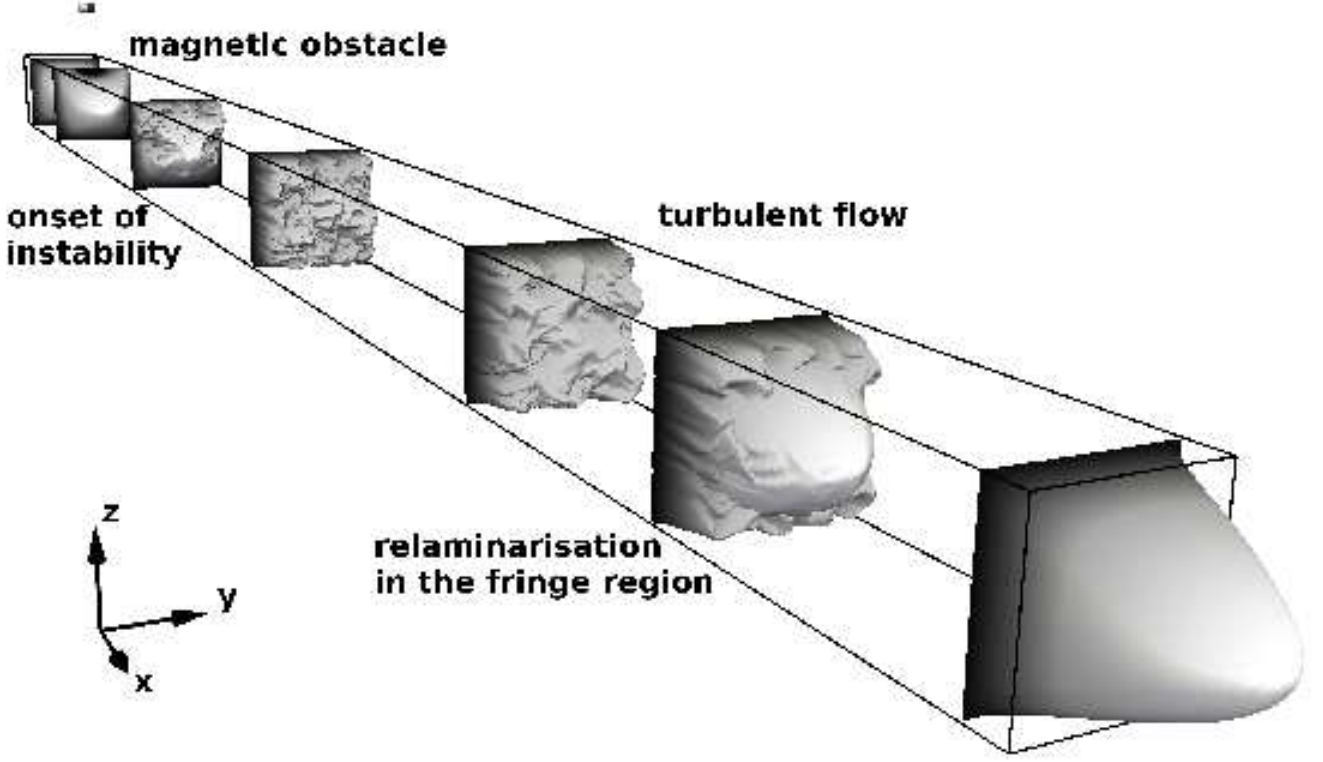


FIG. 3: Sketch of principle of the fringe force method. The incoming laminar flow is deflected by the dipole which acts as a magnetic obstacle. The flow is strongly deformed and can become turbulent in the wake of the dipole. In the region close to the end of the duct, the fringe force relaminarises the flow such that the flow profile is laminar again at the end of the computational domain. This method allows the usage of periodic boundary conditions in the streamwise direction.

end of the domain. For $Re = 100$, a length of 20π was required. This procedure increases therefore the computational cost rapidly when Re is enhanced.

For higher Reynolds numbers, e. g. $Re = 2000$, the flow may become turbulent and this strategy breaks down completely. The conflict with the periodic boundary conditions is circumvented by the application of an additional fringe force which acts in the final downstream section of the duct and relaminarises the transient or turbulent flow⁴⁴. It is sometimes also referred to as the sponge method and is frequently used in studies of turbulent boundary layers^{5,51}.

The fringe method is based on an artificial body force $\vec{F}_{Fringe} = \lambda(\vec{u}_{laminar} - \vec{u})$. This fringe force is added to the right hand side of the Navier-Stokes equations (6). It affects the flow only when the prefactor $\lambda(x)$ is non-zero. The shape of the prefactor function is in our cases given by a step function with smoothed edges⁵. More precisely, it is given by

$$\lambda(x) = \lambda_{max} \left[S \left(\frac{x - x_{start}}{\Delta_{rise}} \right) - S \left(\frac{x - x_{end}}{\Delta_{fall}} + 1 \right) \right]$$

with

$$S(\xi) = \begin{cases} 0, & \xi \leq 0 \\ 0.5 - 0.5 \cos(\xi\pi), & 0 < \xi < 1 \\ 1, & \xi \geq 1. \end{cases}$$

We studied the influence of the parameters, i. e., the maximal amplitude λ_{max} , steepness of the curve in the beginning Δ_{rise} and in the end Δ_{fall} as well as the total length $|x_{end} - x_{start}|$ of the fringe zone. These tests showed that $\lambda(x)$ has to be smooth and periodic. The particular shape is not important. Typical values in the calculation are $\lambda_{max} = 1$,

	$n_x \times n_y \times n_z$	L_x	$\alpha_{y/z}$	$\min\Delta_{y/z}$	$\max\Delta_{y/z}$	$ F_x $	$ I_2(0) $	$ I_4(0) $
$Re = 10,$	★ $1024 \times 96 \times 96$	5π	1.5	0.0064	0.0345	1.1734	0.2390	3.5758
$h = 0.4$	$4096 \times 256 \times 256$	5π	1.5	0.0024	0.0129	1.1497	0.2354	3.5623
$Re = 1000,$	$2048 \times 48 \times 48$	30π	2.0	0.0078	0.0862	0.3050	0.1545	0.1080
$h = 1.6$	$3072 \times 64 \times 64$	30π	2.0	0.0055	0.0647	0.3080	0.1544	0.1089
	$4096 \times 96 \times 96$	30π	2.0	0.0034	0.0432	0.3101	0.1545	0.1096
	★ $2048 \times 96 \times 96$	15π	2.0	0.0034	0.0432	0.3102	0.1545	0.1096
	$6144 \times 128 \times 128$	30π	2.0	0.0024	0.0324	0.3111	0.1547	0.1099
	$8192 \times 192 \times 192$	30π	2.0	0.0016	0.0216	0.3120	0.1550	0.1101
$Re = 2000,$	$1024 \times 48 \times 48$	30π	2.0	0.0078	0.0862	0.1612	0.0386	0.0252
$h = 1.6$	$1728 \times 80 \times 80$	30π	2.0	0.0038	0.0518	0.1635	0.0365	0.0255
	$2048 \times 96 \times 96$	30π	2.0	0.0034	0.0432	0.1639	0.0367	0.0256
	★ $2048 \times 96 \times 96$	15π	2.0	0.0034	0.0432	0.1639	0.0367	0.0256
	$4096 \times 96 \times 96$	30π	2.0	0.0034	0.0432	0.1639	0.0367	0.0256
	$4096 \times 128 \times 128$	30π	2.0	0.0024	0.0324	0.1645	0.0367	0.0256
	$8192 \times 256 \times 256$	30π	1.5	0.0024	0.0129	0.1650	0.0366	0.0257
	$8192 \times 256 \times 256$	30π	1.75	0.0017	0.0145	0.1650	0.0366	0.0257

TABLE I: Results of the resolution study for three different parameter sets with spanwise oriented dipole at $Ha = 100$. The symbol ★ indicates the resolution that is applied in the parameter studies. Properties of the grids are the number of grid points $n_x \times n_y \times n_z$, streamwise length of computational domain L_x , the used the stretching coefficient $\alpha_y = \alpha_z$ in y and z -direction with resulting minimal and maximal grid spacing $\min\Delta_{y/z}$ and $\max\Delta_{y/z}$, respectively. Grid convergence is studied with the streamwise Lorentz force F_x (cf. Eq. (20)), the change of the streamwise momentum flux I_2 and the wall shear stresses I_4 in a cross section at $x = 0$ (cf. Eqns. (16) and (18)). Values for $Re = 2000$ are time-averaged as done in Sec. IV.

$\Delta_{rise} = \pi$, $\Delta_{fall} = \pi/2$ and $|x_{end} - x_{start}| = 3\pi$. Preliminary results with this method were already presented in Tympel et al. (2012)⁵⁶. An example for the resulting velocity profiles is shown in Figure 3. Here, the transformation of the flow by the magnetic dipole for $h = 1.6$, $Re = 3000$ and $Ha = 100$ is illustrated. This computation was performed with $4096 \times 192 \times 192$ grid points in x, y and z directions, stretched with a coefficient of $\alpha_y = \alpha_z = 2$. The streamwise extent of the computational domain is 30π . Due to high computational costs, it is not possible to perform a detailed parameter study with such fine grids.

We performed a grid sensitivity study for three typical parameter sets which are summarized in Table I. In order to resolve the boundary layers and the steep gradients of the magnetic field close to the point dipole properly, we apply a strong grid clustering in y - and z -direction. To elucidate the impact, the corresponding minimal and maximal grid spacing are given. We use three characteristic values to determine whether the resolution is sufficient or not. The first is the total streamwise Lorentz force F_x (cf. Eq. (20)) as it is highly dependent on the velocity and the magnetic field. Second, we compare two integrals over the cross section at $x = 0$: the change of the streamwise momentum flux I_2 and the wall shear stresses I_4 (cf. Eqns. (16) and (18)).

The study confirms that the resolution used in our investigations is sufficient to capture the flow dynamics. For instance in case of $Re = 10$, $Ha = 100$, $h = 0.4$ and a spanwise oriented dipole – which represents the basic setting in Sec. III – the difference between the resulting Lorentz forces of the applied grid with 1024×96^2 and the finest grid with 4096×256^2 points is approximately 2%. For the transient flow at higher Reynolds numbers and the parameter studies in Sec. IV, we attempt to achieve resolutions similar to Gavrilakis (1992)¹⁸ or Huser and Biringen (1993)²⁵. This results in a resolution of 2048×96^2 grid points for a streamwise domain length of 15π . In addition, the total force of this grid is only 0.6% lower than for the finest grid. Furthermore, the resolution study shows that the same physical effects (e.g. the vortex shedding that is described in Sec. IV) are still obtained with a coarser resolution of 1024×48^2 . All values for $Re = 2000$ are time-averaged over 3168 snapshots. To exclude errors due to the time averaging, the grid sensitivity study was repeated for $Re = 1000$. Again, the total force differs only by 0.7 % for the used grid. In addition, the velocity field itself was compared along a line right below the dipole ($x = 0$ and $z = 0.98$): The maximal error is less than 0.1% for all velocity components and less than 0.2% for all components of the Lorentz force density, respectively.

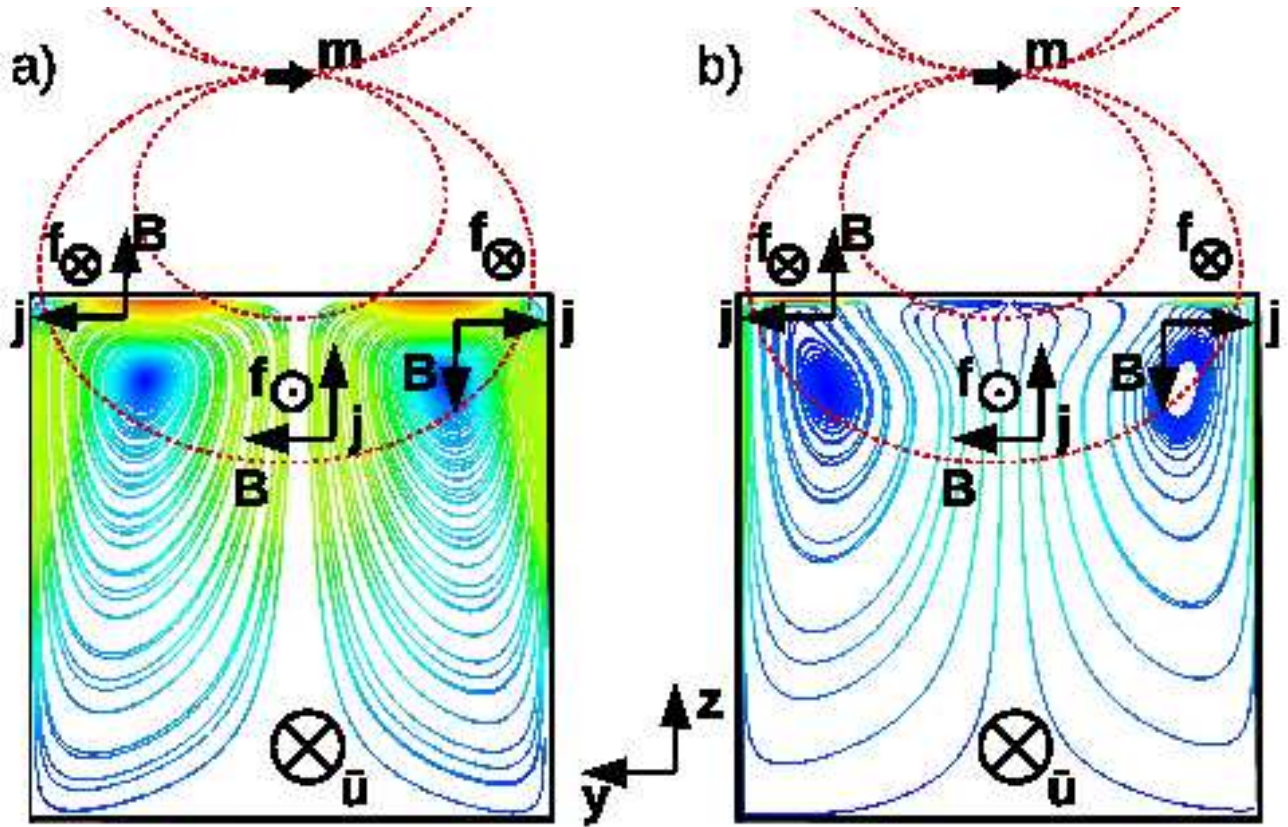


FIG. 4: (colour online) Sketch of principle for the acting forces in case of spanwise oriented magnetic dipole for (a) a laminar base flow and (b) the deflected flow. Streamlines (solid) represent the electric currents in the cross section with $x = 0$ for Reynolds number $Re = 2000$, Hartmann number $Ha = 100$ and dipole distance of $h = 1.6$. Red dashed lines indicate the magnetic field lines. Arrows denote the local main direction of the magnetic field and the currents. In the Hartmann layers (top corners of the duct), the resulting Lorentz force points then in the same direction as the mean velocity. In the centerline, the Lorentz force brakes the fluid and – if strong enough – drives the vortex formation.

III. STATIONARY FLOW AT LOWER REYNOLDS NUMBERS

A. Mechanisms of flow profile deformation

In the following, we discuss the behavior of the flow in case of low Reynolds numbers. As a first step, we take a closer look at the particular deformation of the velocity profile for a Reynolds number $Re = 10$ and a Hartmann number $Ha = 100$. It is observed that differences in the deflection depend on the orientation of the magnetic moment of the dipole.

For low Reynolds numbers, pressure gradient and Lorentz forces balance in the core of the flow provided that the magnetic field is sufficiently strong. This solution is usually not compatible with the conditions at walls. When the magnetic field has a sufficiently strong wall-normal component, the tangential force balance at a wall gives rise to an electromagnetic boundary layer called Hartmann layer. The velocity difference across this layer is related to an electric current parallel to the wall and perpendicular to the outer velocity⁵⁰. Hartmann layers can be formed whenever their thickness is small compared with the lateral variation of the flow and magnetic field. Their appearance is therefore not restricted to uniform fields.

In the problem at hand, the Hartmann layers are regions where the velocity at the outer edge is controlled by the current in the layer. These currents in the Hartmann layers are generated by the electromotive force $\vec{u} \times \vec{B}$ in the core. Since the flow is dominated by the streamwise velocity component, we can infer the current pattern from the distribution of the magnetic dipole field. The Hartmann layers then typically indicate a local acceleration of the flow, which affects the velocity distribution in its vicinity. In the following, we shall focus on the characteristic current

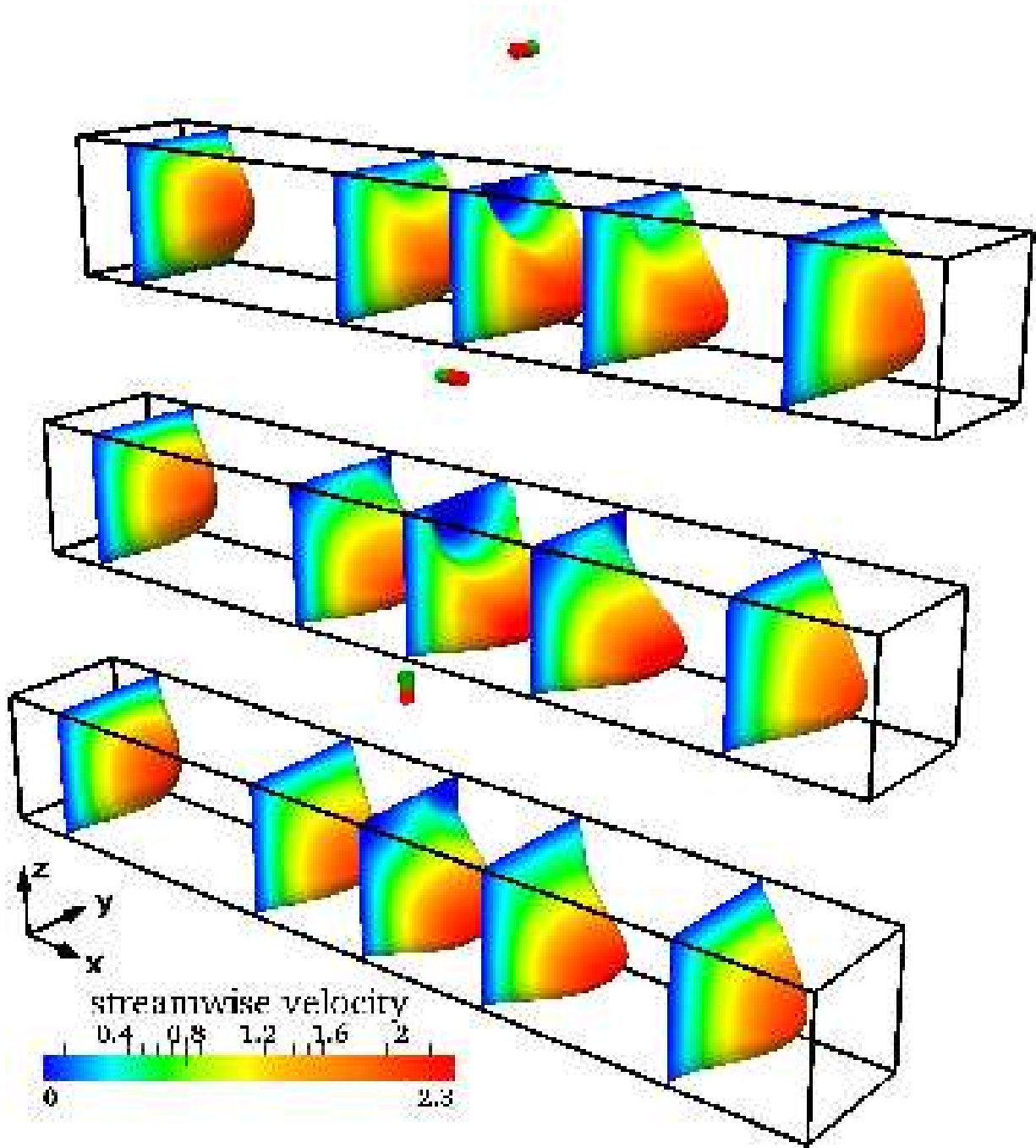
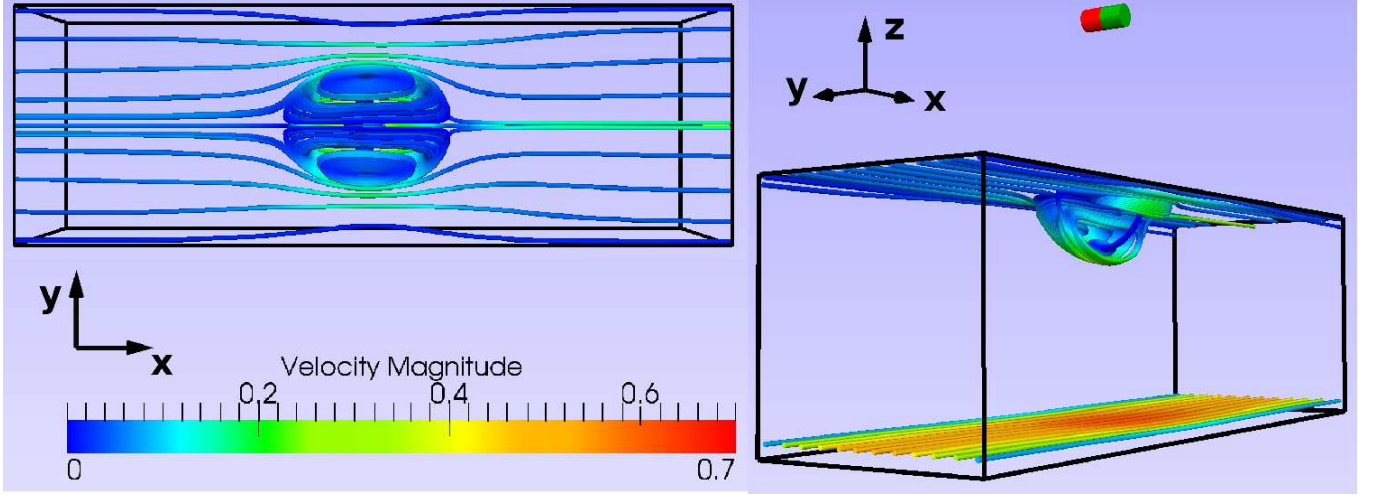


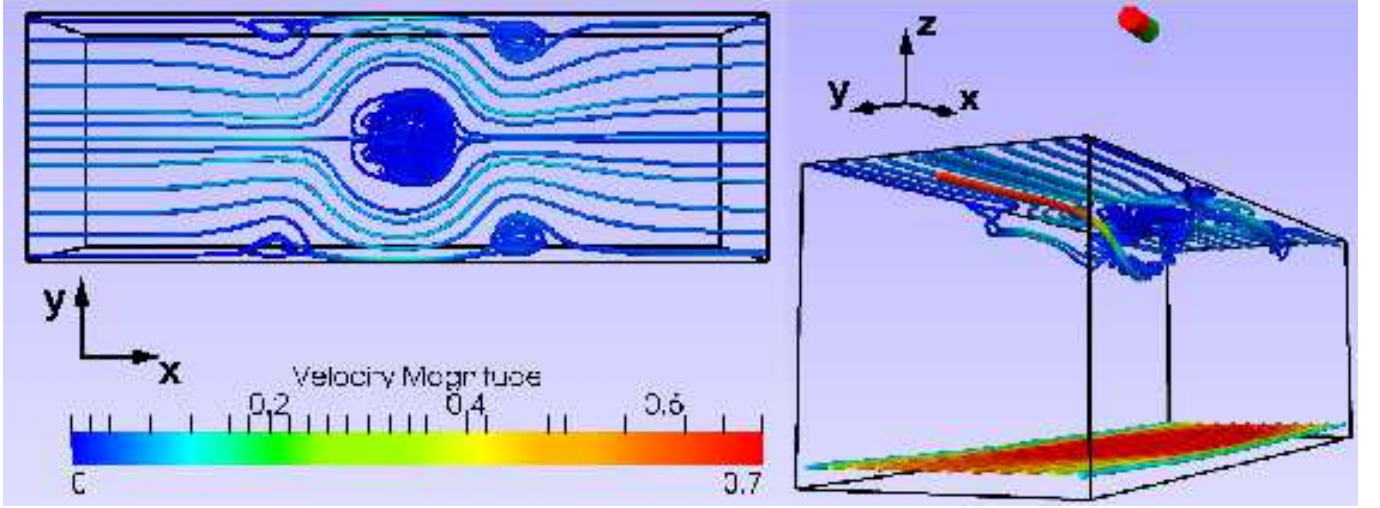
FIG. 5: The point dipole as a magnetic obstacle: Contours of streamwise velocity at various positions along the duct illustrate the effect of a point dipole on the duct flow dynamics. From left to right: $x = -3, -1, 0, 1, 2.5$. Total duct length is 5π and $Re = 10$, $Ha = 100$, $h = 1.6$. Three different orientations of the dipole are presented: top – spanwise, middle – streamwise and bottom – vertical magnetic moment

distribution for a velocity field dominated by the streamwise component. The associated Lorentz forces and Hartmann layers for this current distribution indicate how the flow field is transformed.

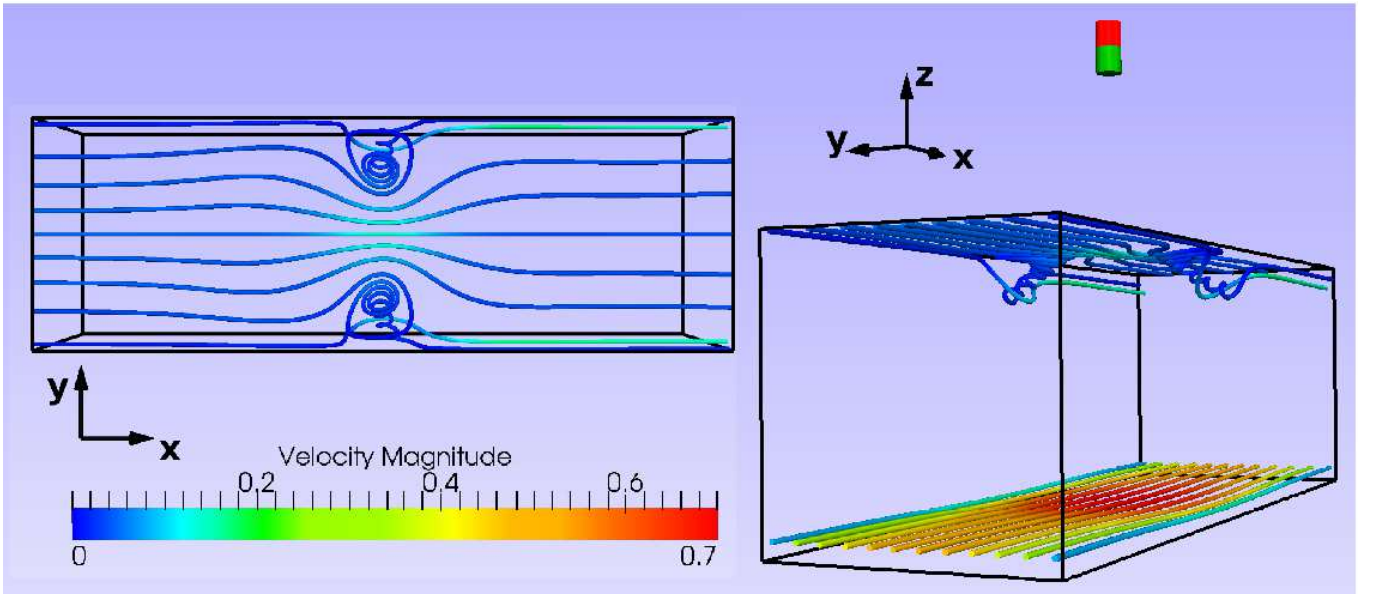
Let us consider the case of a magnetic dipole in spanwise direction, i. e., $\vec{m} \parallel \vec{e}_y$. The magnetic field is perpendicular to the flow direction and parallel to the top wall when the dipole is not too close to the duct. The magnetic field is of high magnitude and strongly inhomogeneous in the cross section directly below the dipole, i. e., at $x = 0$ (Fig. 4). The induced current density is the result of the electromotive force $\vec{u} \times \vec{B}$ and the induced electric field represented by the gradient of the electric potential. In the bulk, the currents qualitatively conform to the electromotive force



(a)



(b)



(c)

FIG. 6: (colour online) Velocity field streamlines for different orientations of the dipole at $Re = 10$, $Ha = 100$, $h = 1.6$. Dipole orientations are a) spanwise, b) streamwise, c) vertical. The local Hartmann layer is visible due to higher velocities at the top surface. Vortices and flow structures are always three-dimensional. All three configurations are shown from two different perspectives in each case: left is a top view and right a side view. The box indicates the duct from $x = -3$ to $x = 3$. The total length of the duct was 5π .

$\vec{u} \times \vec{B}$. Differences arise near the walls where the currents have to close because of $\nabla \cdot \vec{j} = 0$. Figure 4 (a) shows that there are two stagnation points in the streamline pattern of the electric currents based on the laminar velocity distribution. They are close to the surface. Figure 4 (b) shows that the essential properties of the current distribution are preserved for the modified flow field. The streamlines have been obtained from a numerical simulation and are projected into the cross section. What may look like a sink or a source in Fig. 4 (b) can be explained as a result of the projection on the two-dimensional cross section.

With the obtained current density, one may now estimate the resulting Lorentz force distribution $\vec{f} \sim \vec{j} \times \vec{B}$ in the duct which will result in a braking force in the bulk of the flow. It should be emphasized that this braking force is also present in the region directly below the dipole. Here, the magnetic field has the largest magnitude. If this force is strong enough, which is the case when the Hartmann number is sufficiently large, a local flow reversal is observed. The resulting vortices in Figs. 5 (top) and 6 (a) mark now the areas with strong spanwise magnetic field. In the top corners, the situation is different. As the current density field lines close here, the resulting Lorentz force accelerates the flow. Thus, local Hartmann layers are created. These layers are of interest when the influence of the Hartmann number is investigated in Sec. IV C. Contrary to the classical Hartmann flow configuration^{21,22}, the local Hartmann layer is present at the top wall and practically absent at the bottom wall. As a consequence, the flow distortion decreases rapidly when moving from the top to the bottom wall. This is illustrated in Fig. 6 by a second set of streamlines seeded at a distance of 0.05 length units above the bottom wall. Nonetheless, local Hartmann layers also appear for the other dipole orientations where the normal component of the magnetic field is sufficiently strong at a wall. In case of a streamwise dipole orientation, strong Hartmann layers are found at the centerline ahead and behind the dipole position. Much less pronounced layers are also found at the sides.

For the same reasons, one observes a well pronounced local Hartmann layer positioned directly below a vertical dipole, i. e., $\vec{m} \parallel \vec{e}_z$. Here, the main component of the magnetic field is in vertical direction and thus perpendicular to the flow direction and to the top wall. These layers can be observed in Figs. 5 (bottom) and 6 (c). In addition, two vortices are created in the top corners. One may understand the case of the vertical dipole as counterpart of the spanwise case as it forms Hartmann layers where the other shows areas of reversed flow and vice versa. Moreover, the vertical dipole induces spanwise oriented currents in the bulk as it is the case for a homogeneous vertical field. Consequently, the total Lorentz force appears again as a braking force.

In the case of streamwise magnetic moment, i. e., $\vec{m} \parallel \vec{e}_x$, one observes five well pronounced vortices at the top as shown in Fig. 6 (b). The four small vortices in Fig. 6 (b) are located up- and downstream of the dipole at positions where local Hartmann layers appear along the centerline. In this region, the currents in the bulk are in the spanwise direction. They close near the upper and lower walls. This is the reason for a braking Lorentz force near the lateral walls by the spanwise component of the magnetic field. At the centerline, the flow is accelerated in the Hartmann layer. This Lorentz force distribution causes regions of reversed and accelerated flow. The strongly pronounced vortex directly below the dipole is not directly generated by the magnetic field. The main component of the magnetic field in this area is a streamwise component and thus parallel to the mean flow direction and the top wall. A streamwise magnetic field cannot produce an electric current and therefore the action of the Lorentz force vanishes right below the streamwise oriented dipole. Nevertheless, vortices like the one just discussed have been observed for the streamwise oriented dipole at several Reynolds numbers and strong Hartmann numbers. The origin of this vortex may be found in the local Hartmann layers that surround the vortex. The Lorentz forces affect the liquid at the top as follows. The flow is first accelerated at the centerline, then pushed aside to the two Hartmann layers close to the edges and finally again accelerated at the centerline. This forcing leaves the liquid right below the dipole no other possibility, but to swirl and to form a vortex. One has to mention here that this explanation is more or less descriptive and that the flow is always fully three-dimensional as indicated in Figs. 6 (b).

An alternative explanation of the flow modification might be given by means of the characteristic surfaces in creeping magnetohydrodynamic flows, which have been introduced by³⁷. These surfaces can be defined when pressure gradient and Lorentz force balance in the core of the flow. They are spanned by the parts of the magnetic field lines within the flow that have a constant value of the line integral $\int ds / \|\vec{B}\|$. Under certain additional assumptions, the flow will be parallel to these surfaces^{3,4}. One may therefore expect the flow to avoid the regions enclosed by field lines with a certain magnitude of the magnetic field. For the stream- and spanwise orientations this would be a roughly hemispherical region directly beneath the dipole. For the vertical dipole orientation, there would be two such domains to the left and to the right of the dipole. This is also in qualitative agreement with the specific arguments based on the current distribution that we have discussed before.

So far, we have reported the velocity profiles and the streamlines of the flow. These plots give us information on the flow structures, but not on the Lorentz force components in the flow. In order to proceed, we quantify the influence of the dipole on the flow with an integral criterion for the balance of Lorentz force, pressure gradient and wall stresses. Such a balance equation is obtained directly from the Navier-Stokes equation (6). We integrate the x -component of (6) with respect to y and z and apply the assumptions that the velocity field is smooth and stationary and that

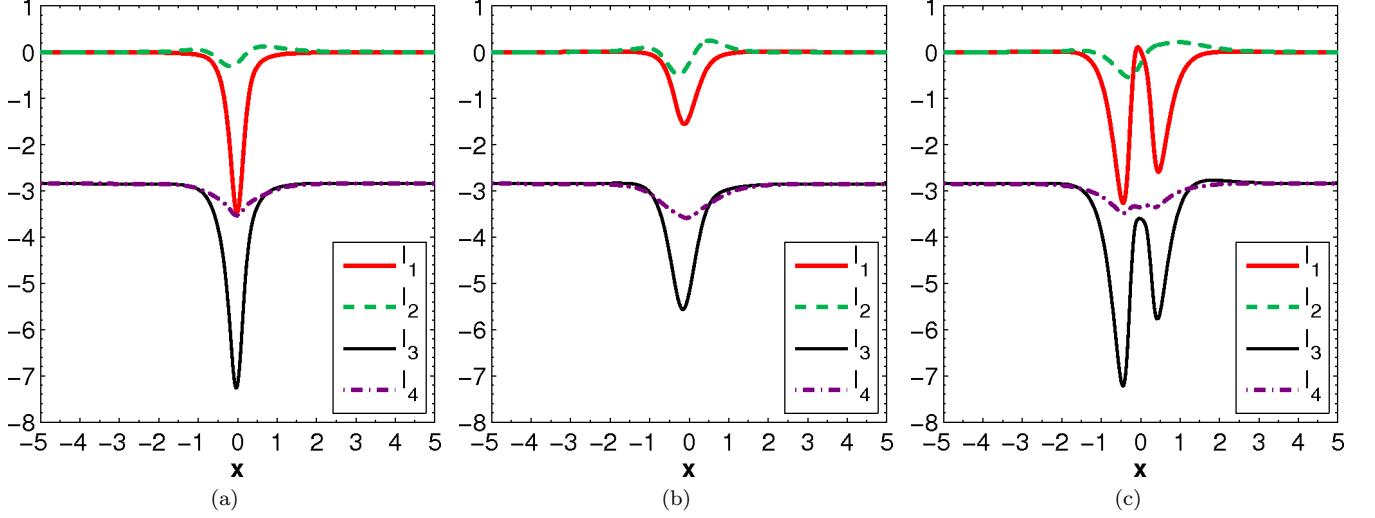


FIG. 7: (colour online) Terms of the integrated momentum balance as given by Eqns. (15) to (18) at $Re = 10$, $Ha = 100$, $h = 0.4$. Streamwise profiles for different dipole orientations are shown: (a) vertical, (b) spanwise, (c) streamwise.

the volume flux is constant and normalized to 1. The balance equation is

$$I_1 + I_2 - I_3 + I_4 = 0. \quad (14)$$

It contains the Lorentz force term

$$I_1 = \iint_{[-1,1]^2} f_x dy dz, \quad (15)$$

the change of the streamwise momentum flux

$$I_2 = - \iint_{[-1,1]^2} \partial_x (u_x^2) dy dz, \quad (16)$$

the friction coefficient

$$I_3 = \iint_{[-1,1]^2} \partial_x p dy dz \quad (17)$$

and the contribution of the wall shear stresses

$$I_4 = \frac{1}{Re} \left(\int_{-1}^1 [\partial_y u_x]_{y=\pm 1} dz + \int_{-1}^1 [\partial_z u_x]_{z=\pm 1} dy \right). \quad (18)$$

For a homogeneous magnetic field, the integral of the Lorentz force per cross section vanishes. In case of a laminar flow, wall stresses are balanced by the pressure gradient. With an inhomogeneous magnetic field present, the question of which hydrodynamic forces balance the appearing Lorentz forces arises. Figure 7 shows all terms of the balance equation (14) for the three dipole orientations.

We can see that the contribution to the Lorentz force is mainly based on the presence of the local Hartmann layers. Therefore, the forces are much stronger for the vertical case than for the spanwise one. The strongest contribution of the Lorentz force comes from the streamwise oriented dipole. Here, two Hartmann layers are clearly visible, ahead and behind the dipole positioned at $x = 0$. It also becomes clear that it is mainly the pressure gradient which balances the Lorentz force. The nonlinear term I_2 is small due to the low Reynolds number of $Re = 10$. In Sec. IV, we will come back to this point and will see that the nonlinear term has a stronger influence as expected for higher Reynolds numbers. Before increasing the Reynolds number, we study the influence of the Hartmann number at fixed $Re = 10$.

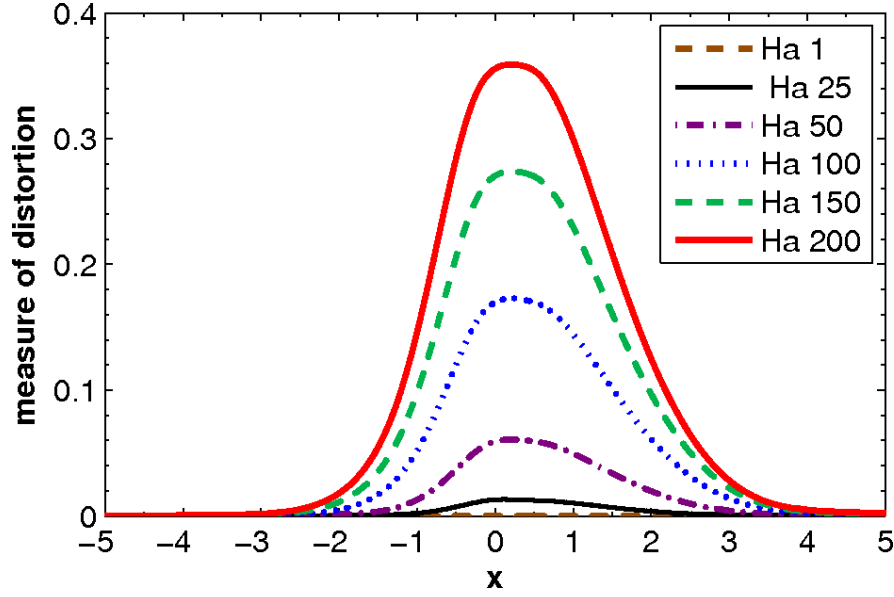


FIG. 8: (colour online) Distortion of the laminar duct flow as a function of the Hartmann number for a low Reynolds number duct flow at $Re = 10$. Deflection of the flow in dependence of Hartmann number as quantified by \mathcal{A} .

B. Hartmann number dependence at fixed Reynolds number

The following scalar integral measure

$$\mathcal{A}(x) = \frac{\iint |\vec{u} - \vec{u}_{lam}| dy dz}{\iint |\vec{u}_{lam}| dy dz}. \quad (19)$$

will be used for quantification of the distortion of the laminar profile \vec{u}_{lam} caused by the magnetic obstacle. An example for the distortion is shown in Fig. 8 for a Reynolds number of 10 and a wall-normal oriented dipole in a distance $h = 0.4$. The graphs compare the distortion for several Hartmann numbers which are indicated in the legend. Two effects are observed. First, there is almost no distortion of the flow for $Ha < 25$. In this range, the resulting forces behave to a good approximation as in the kinematic case for an unperturbed flow. They are also comparable with the experiments by Heinicke et al. (2012)²⁴ in this parameter range. Second, the maximal amplitude of \mathcal{A} increases approximately linearly with the Hartmann number for $Ha > 25$. Nevertheless, one can assume a saturation of this deformation for very high Hartmann numbers due to the finite duct geometry. Furthermore, the starting point of the deflection is shifted upstream with increasing Hartmann number. In particular, it changes from $x \approx -1$ for $Ha = 25$ to $x \approx -3$ for $Ha = 200$. In all cases the distortion subsides at approximately four characteristic lengths downstream of the dipole position. Therefore, the curves become slightly more symmetric for higher Hartmann numbers.

Let us now focus on the integral forces and torques. Therefore, we define the total Lorentz force by

$$\vec{F} = \int_V \vec{f} dV = \int_V \frac{Ha^2}{Re} (-\nabla\phi + \vec{u} \times \vec{B}) \times \vec{B} dV, \quad (20)$$

and the total torque as

$$\vec{T} = \int_V \vec{r} \times \vec{f} dV \quad (21)$$

with $\vec{r} = \vec{x} - (h+1)\vec{e}_z$. Calculations are done for the three main dipole orientations. The dependence of the integral forces on Reynolds and Hartmann number was found to be practically the same for all orientations. More interestingly, the absolute values of the forces were found to differ at the same values of Hartmann and Reynolds numbers. The streamwise oriented dipole gave always stronger forces than the wall-normal vertical one. It has to be recalled that the Hartmann number is based on B_{max} , the maximal value of the magnetic field inside the duct, and not on the magnetic moment of the dipole. Thus, in an experiment using a real magnet, it is always found that a rotation of the magnetic dipole from vertical to streamwise orientation will cause a decrease of the forces simply because such

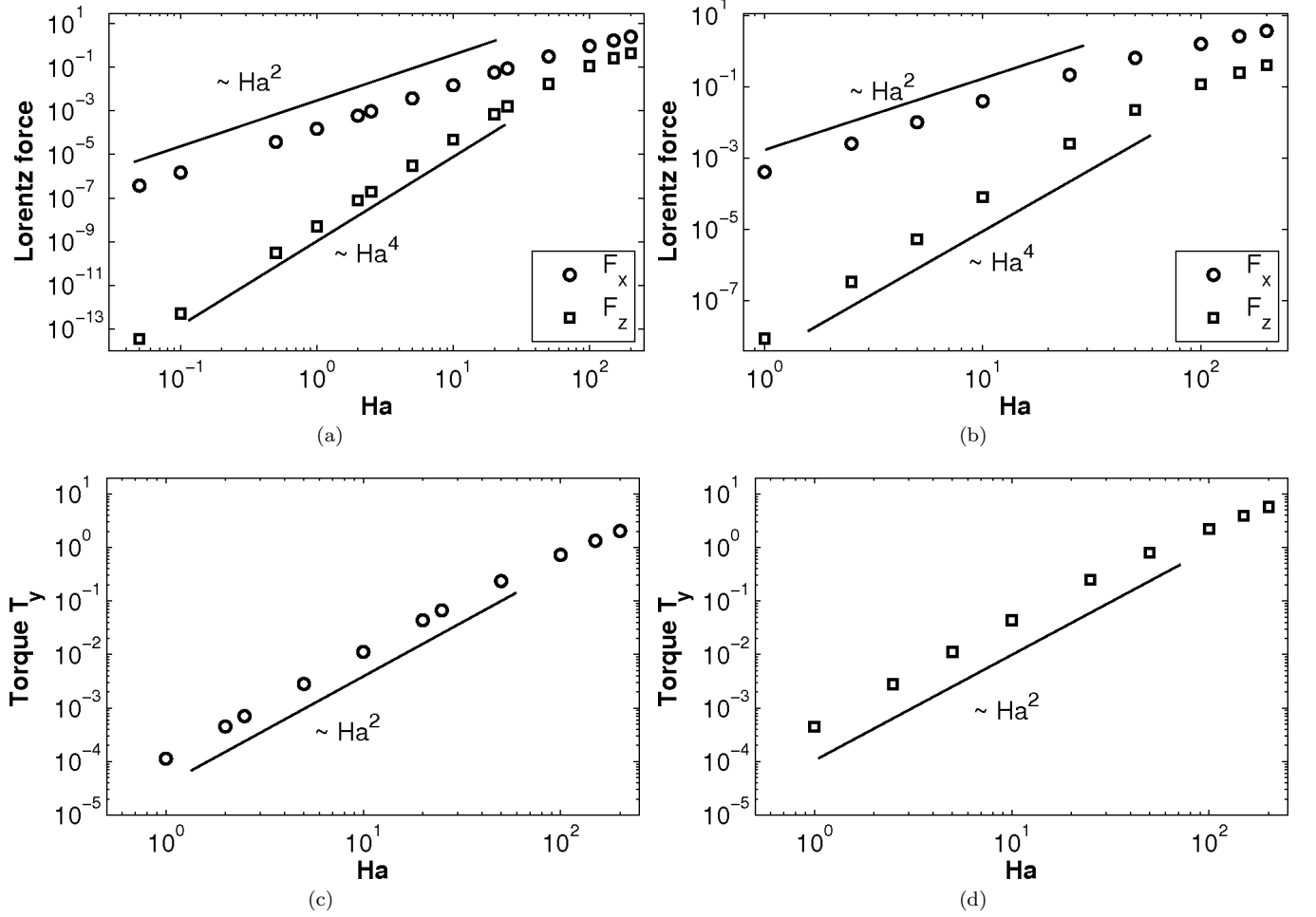


FIG. 9: Drag and lift forces and resulting torque as a function of the Hartmann number for $Re = 10$ and $h = 0.4$. (a,c) wall-normal orientation of the dipole. (b,d) streamwise orientation of the dipole.

a rotation will decrease the Hartmann number by a factor of two in correspondence with Eq. (2). In all cases, the spanwise oriented dipole will give the weakest force. The integral torque component behaves in the same way as the forces. The torque is zero for the spanwise dipole orientation due to the symmetry of the problem.

In Fig. 9, we compare the total drag force, i. e., the streamwise force component, the total lift force i. e., the vertical force component (upper panels), and the total torque (lower panels) for the wall-normal and streamwise dipole. We observe that the drag force is higher than the lift force. The data in Fig. 9 reveal three power laws which seem to be valid up to $Ha \approx 25$. For higher Hartmann number values the growth with Ha becomes weaker. As expected, one finds that the drag force $F_x \sim Ha^2$ and that the torque component $T_y \sim Ha^2$. These power laws are caused by the fact that Ha^2/Re is a prefactor to the Lorentz force term in the momentum balance. The third power law for the lift force is found as $F_z \sim Ha^4$. This behavior of the lift force is not immediately obvious. We explain it by the following argument.

Let \vec{u} be a solution to the Navier Stokes equation (6) for a given Hartmann and Reynolds number. Similar to a perturbation expansion in weakly nonlinear flows, we divide the velocity field in three parts,

$$\vec{u} = \vec{u}_0 + \vec{u}_1 + \vec{u}_2. \quad (22)$$

Here, \vec{u}_0 is the base flow, \vec{u}_1 describes the distortion of the base flow and \vec{u}_2 stands for a higher-order nonlinear term. The base flow \vec{u}_0 is the flow in the limit of small interaction parameter Ha^2/Re and low Reynolds number. It is supposed to be a steady flow which is solely driven by the pressure gradient. Thus, \vec{u}_0 is the solution of

$$0 = -\nabla p + \frac{1}{Re} \nabla^2 \vec{u}_0. \quad (23)$$

This solution is the laminar flow \vec{u}_{lam} which can be derived analytically⁴⁵. As it was shown in²⁴, the Lorentz forces for a given laminar profile and for the full Navier-Stokes equation (6) are almost the same in case of Hartmann and Reynolds numbers below certain thresholds. The present case of $Ha = 25$ and $Re = 10$ satisfies these thresholds and the approximation with a laminar profile \vec{u}_{lam} gives a good agreement for the drag component of the Lorentz force. However, the lift force is zero for a laminar velocity profile.

The second term \vec{u}_1 describes the deflection due to the dipole. It is again an approximation which holds for small Reynolds numbers. Again, this flow is steady. Viscous forces are balanced by the Lorentz force

$$\frac{1}{Re} \nabla^2 \vec{u}_1 \approx -\frac{Ha^2}{Re} (-\nabla \phi_0 + \vec{u}_0 \times \vec{B}) \times \vec{B}. \quad (24)$$

It is clear from this equation that the amplitude $u_1 \sim Ha^2$. We note that an additional pressure correction is necessary to maintain incompressibility. The contribution \vec{u}_1 does not give a contribution to the lift force. This can be shown with the following argumentation based on Stokes flow. Assume that there is a non-zero lift force F_z . On the one hand, the linearity of the equations implies that a sign reversal of pressure and $\vec{u}_0 + \vec{u}_1$, respectively, results in an opposite force. In particular, the lift force would reverse, i. e., one would obtain $-F_z$. On the other hand, the problem has mirror symmetry with respect to the (y, z) plane containing the dipole, i. e., a reversal of flow direction should change the sign of the drag force F_x but not the sign of the lift force. For this reason $F_z = -F_z$, i. e., the lift force has to vanish.

The third part of the decomposition, \vec{u}_2 , is the nonlinear part which mainly reflects effects of inertia. This term is an approximation, but presents the realistic flow pattern for moderate Reynolds numbers. Rewriting Eq. (22) to $\vec{u}_2 = \vec{u} - \vec{u}_0 - \vec{u}_1$ in the Navier-Stokes equation (6) for the steady flow case and neglecting all terms of order $O(Ha^4)$ leads to

$$\nabla^2 \vec{u}_2 = Re ((\vec{u}_1 \cdot \nabla) \vec{u}_0 + (\vec{u}_0 \cdot \nabla) \vec{u}_1). \quad (25)$$

From this equation, one can estimate that $u_2/\ell^2 \approx Re u_1 u_0/\ell \approx Re Ha^2 u_0^2 \ell$. Thus, $u_2 \approx Re Ha^2 u_0^2 \ell^3$ which gives rise to the lift force $F_z \approx (Ha^2/Re) u_2$ and thus the expected Hartmann number dependence of Ha^4 for the lift force. We denoted in this estimate by ℓ the nondimensional characteristic gradient variation scale given in units of the duct half width. It was also numerically verified that the lift force vanishes when the nonlinear term $(\vec{u} \cdot \nabla) \vec{u}$ is artificially set to zero. In this case, the flow was symmetric in streamwise direction. Thus, the numerical test confirms that the nonlinear term is responsible for non-symmetric pattern in the flow and for the lift force. We also note that a more formal argument could be given using a double expansion in the two small parameters Ha and Re .

C. Reynolds number dependence at fixed Hartmann number

Besides the Hartmann number, the second control parameter, Re , will affect the structures of the flow. Following directly from the definition of the Lorentz force, we verify the dependencies $F_x \sim 1/Re$ and $T_y \sim 1/Re$, respectively, which are shown in Fig. 10 for several Hartmann numbers. Furthermore, we see that the lift force F_z is constant at a given Hartmann number for $Re < 1$ as already discussed above. In case of higher Reynolds number, the lift force data decay steeper than $1/Re$.

With increasing Reynolds number the contributions of the nonlinear advection term will increase and manifest in an increasing distortion of the flow. We observe that the distortion in the wake, as measured by Eq. (19), decays almost exponentially, i. e., as a function $\exp(-\alpha x)$ with respect to the streamwise direction obeying a spatial decay rate α . This is demonstrated in Fig. 11 for a Hartmann number of $Ha = 100$ in a logarithmic-linear plot. The first observation is that the maximum of the distortion is decreasing with increasing Reynolds number – an effect of the decaying interaction parameter Ha^2/Re . The decay of the maximal value may also be considered as an effect of the nonlinear term. A numerical test case shows that the value does not decrease if the nonlinear term is artificially switched off. When the data are presented in a logarithmic scale, as in the lower right panel of Fig. 11, the exponential decay is clearly visible. The fit of these data with an exponential function results in a spatial decay rate which is approximately inversely proportional to the Reynolds number.

The Reynolds number dependence of the decay rate can be rationalized from the following consideration for steady flow. The Lorentz force term $(Ha^2/Re)(\vec{j} \times \vec{B})$ is a localized force term and will not affect the decay in the wake sufficiently far downstream from the dipole position, i. e., we can drop it in the wake. The Navier-Stokes equations simplify to

$$(\vec{u} \cdot \nabla) \vec{u} = \frac{1}{Re} \Delta \vec{u} - \nabla p. \quad (26)$$

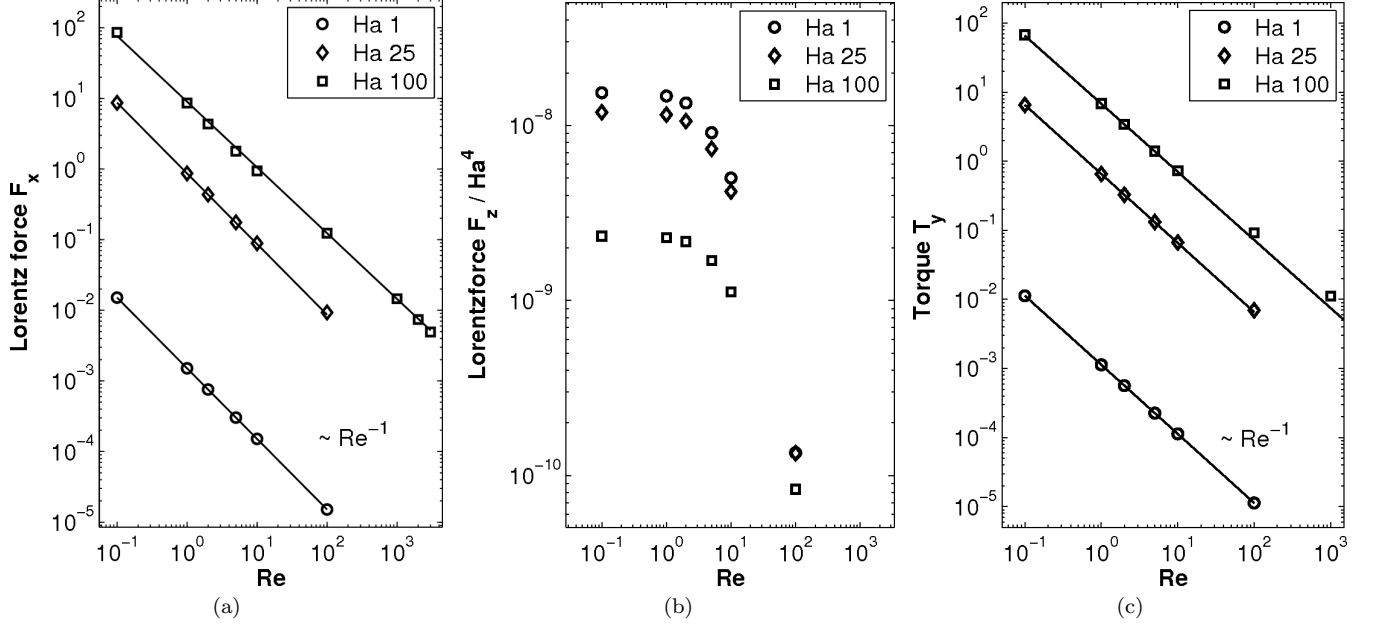


FIG. 10: Reynolds number dependence of the force components and the torque. (a) drag force F_x ; (b) lift force F_z compensated by Ha^4 ; (c) torque T_y . Data are for a wall-normal magnetic point dipole at a distance of $h = 0.4$. The dependence $1/Re$ is indicated by a solid line for the drag component of the Lorentz force and the torque. Data are obtained for several Hartmann numbers as indicated in the legend.

We now represent the distortion as $\vec{v} = \vec{u} - \vec{u}_{lam}$. If we use this representation, then the dominant term on the left hand side becomes $u_{lam}\partial_x\vec{v}$. On subtracting the equation for the laminar flow itself we obtain

$$u_{lam}\partial_x\vec{v} = \frac{1}{Re}\Delta\vec{v} - \nabla p', \quad (27)$$

where the pressure contribution p' serves to maintain incompressibility. If we further approximate the laminar velocity distribution by its mean value \bar{u} we eventually have

$$\bar{u}\partial_x\vec{v} = \frac{1}{Re}\Delta\vec{v} - \nabla p'. \quad (28)$$

Following usual boundary-layer approximation ideas based on $Re \gg 1$ one can further neglect the second derivative with respect to x in the Laplacian. The problem then effectively reduces to a diffusion problem

$$\partial_t\vec{v} = \frac{1}{Re}\left(\frac{\partial^2}{\partial y^2} + \frac{\partial^2}{\partial z^2}\right)\vec{v} \quad (29)$$

where we have introduced $t = x/\bar{u}$. Using separation of variables, it is clear that the decay of $|\vec{v}|$ with t is ultimately determined by the largest eigenvalue $-\alpha_1$ of the two-dimensional Laplacian, i. e.,

$$|\vec{v}| \sim \exp(-\alpha_1 t/Re) = \exp(-\alpha_1 x/Re\bar{u}). \quad (30)$$

Therefore, the measure of distortion has to decay approximately exponentially. The last steps of our argumentation are more heuristic because we neglect the remaining pressure term. A justification of this step might be not straightforward, but we suppose that it is justified because it amounts to a projection on the space of solenoidal functions, which should not interfere with the gist of the argument. We further note that the spatial decay is independent of the orientation of the magnetic dipole. The numerical simulations show that this is approximately the case for $Ha = 100$ and Re reaching from 10 up to 2000. We also remark that the decay is clearly visible only at large distances from the dipole position. For $Re \gtrsim 500$, it is difficult to identify a clear exponential decay of $\mathcal{A}(x)$ (cf. Eq. 19) within the computational domain because of the slower decay of higher modes.

To summarize the results for the lower Reynolds numbers: we explained why different transformations of the flow are observed for different dipole orientations leading to the formation of local Hartmann layers and areas of reversed

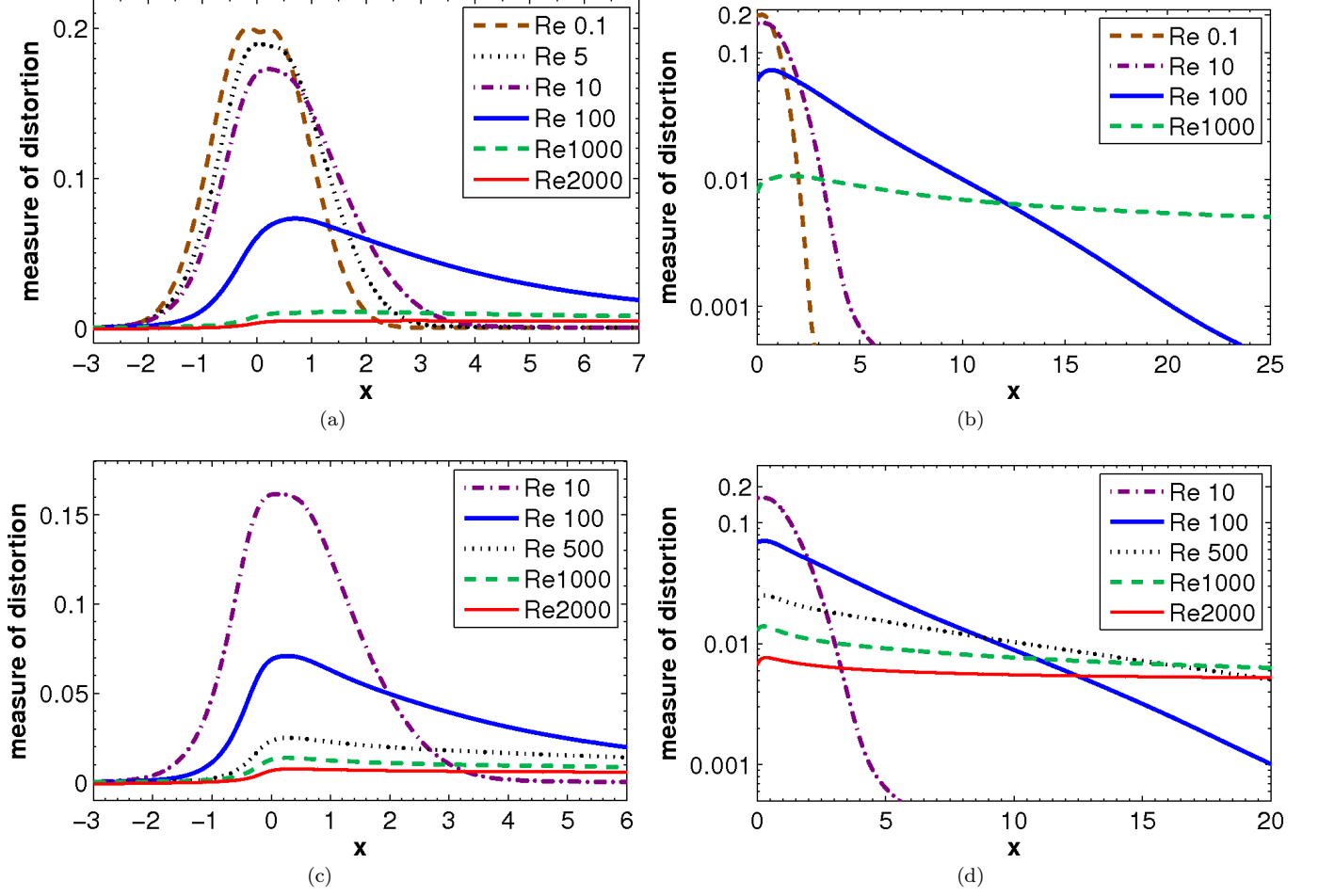


FIG. 11: (colour online) Flow distortion as quantified by Eq. (19) for several Reynolds numbers. In all cases, $Ha = 100$ and $h = 0.4$. The dipole is located at $x = 0$ with (a) wall-normal magnetic moment and (c) spanwise magnetic moment, respectively. Panels (b) and (d) replot the same data on logarithmic-linear axes.

flow due to strong Lorentz forces. The strength of the forces and their effect on the deflection of the flow in dependence on the Hartmann number was also analyzed. The total drag force is found to be proportional to Ha^2 and the total lift force is proportional to Ha^4 in the present Reynolds number regime. When the Reynolds number is increased, we observe that the length of the wake is increased. It was also shown why the spatial downstream decay of the deflected flow in the wake is proportional to $1/Re$. In the next section, we will see how the vortex formation process changes when the dipole triggers a transition to turbulence as the Reynolds number is increased.

IV. TIME-DEPENDENT FLOW AT HIGHER REYNOLDS NUMBERS

In this section, we study time-dependent flow structures which start to appear at Reynolds numbers of about 2000 and higher and for Hartmann numbers above 80. We will observe vortex shedding for cases when the dipole is positioned sufficiently far in a distance of $h = 1.6$ from the top surface of the liquid. For smaller distances than $h = 1.0$ the flow is always stationary in the range of Reynolds numbers which could be covered here ($Re \leq 3000$). Therefore, we will restrict our study in this section to the case with $h = 1.6$ which generates qualitatively new features compared to the last section.

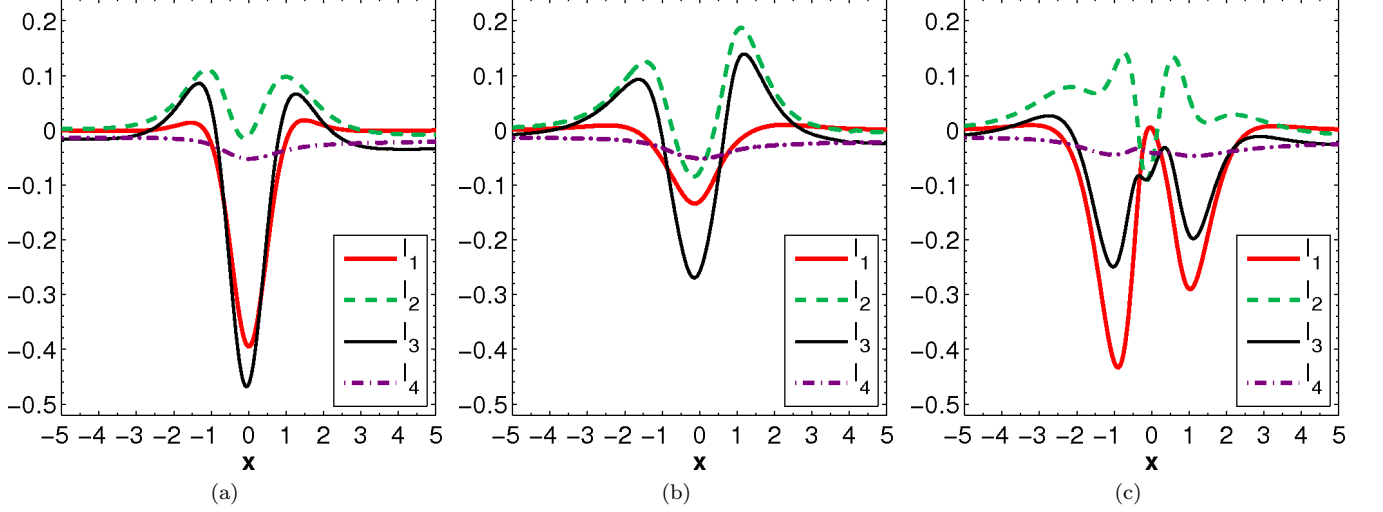


FIG. 12: (colour online) Streamwise variation of the different terms of the momentum balance (14) averaged over the cross section at $Re = 2000$, $Ha = 100$, $h = 1.6$ for three different orientations of the dipole: (a) wall-normal vertical, (b) spanwise, (c) streamwise. Equations (15) to (18) have been used again. Since the spanwise case in the mid panel is time dependent, data are time-averaged over one oscillation time of 3.168 time units.

A. Deformation of the flow

The analysis of the different contributions to the momentum balance (14) is shown in Fig. 12 for $Re = 2000$ and $Ha = 100$ for the three dipole orientations: streamwise, spanwise and wall-normal vertical. The deformations of the flow field show effects which are similar to the low Reynolds number case from Sec. III. Since the Reynolds number is higher, the nonlinear term has a stronger influence on the deflection of the flow as visible by its larger magnitude in the figures. The terms of the momentum balance (14) reveal that the Lorentz force obeys a qualitatively similar behavior as in the low Reynolds number cases (cf. also Fig. 7). It is again the pressure gradient that balances the additional contribution that is now produced by the change of streamwise momentum flux I_2 .

The velocity field streamlines for the three cases are shown in Fig. 13. We observe again the formation of local Hartmann layers and vortices as described for the low Reynolds number runs in Sec. III. In case of the spanwise oriented dipole, a strong vortex in the center of the duct is formed which becomes now time-dependent, i.e., a vortex shedding is initiated. For streamwise and wall-normal oriented dipoles the flow in the wake remains stationary due to the local Hartmann layers that stabilize the flow in the range of Reynolds numbers accessible here.

Stability investigations for the onset of time-dependent flow become less straightforward as the base flow depends on the Hartmann number. Thus, a simplified criterion for two-dimensional flow is applied here. A possible explanation for the instability and transition to a time-dependent flow is shown in Fig. 13. In the right column of the figure, we show five cross sections that contain the magnitude of the cross-stream gradient of the streamwise velocity which is determined by $\vec{\nabla}_2 u_x$ where $\vec{\nabla}_2$ denotes the gradient with respect to y and z directions. Furthermore, the inflection point criterion⁵⁷ follows with the definition

$$\vec{n} = \frac{\vec{\nabla}_2 u_x}{|\vec{\nabla}_2 u_x|} \quad (31)$$

to

$$\vec{\nabla}_{\vec{n}}^2 u_x = 0. \quad (32)$$

Criterion (32) generalizes the inflection points in one-dimensional velocity profiles. It has been used frequently in order to determine whether a flow can become unstable or not. Contour lines which satisfy (32) are added to each of the five cross section plots in Fig. 13. We observe that in case of a spanwise oriented dipole the magnitude of the gradient close to the inflection line is higher compared to the other cases. Thus the probability of instability increases. As a consequence, we will restrict our observations and parameter studies in this section to the spanwise oriented dipole, the most interesting case for transition to turbulence. In the subsequent paragraph, we will be concerned with

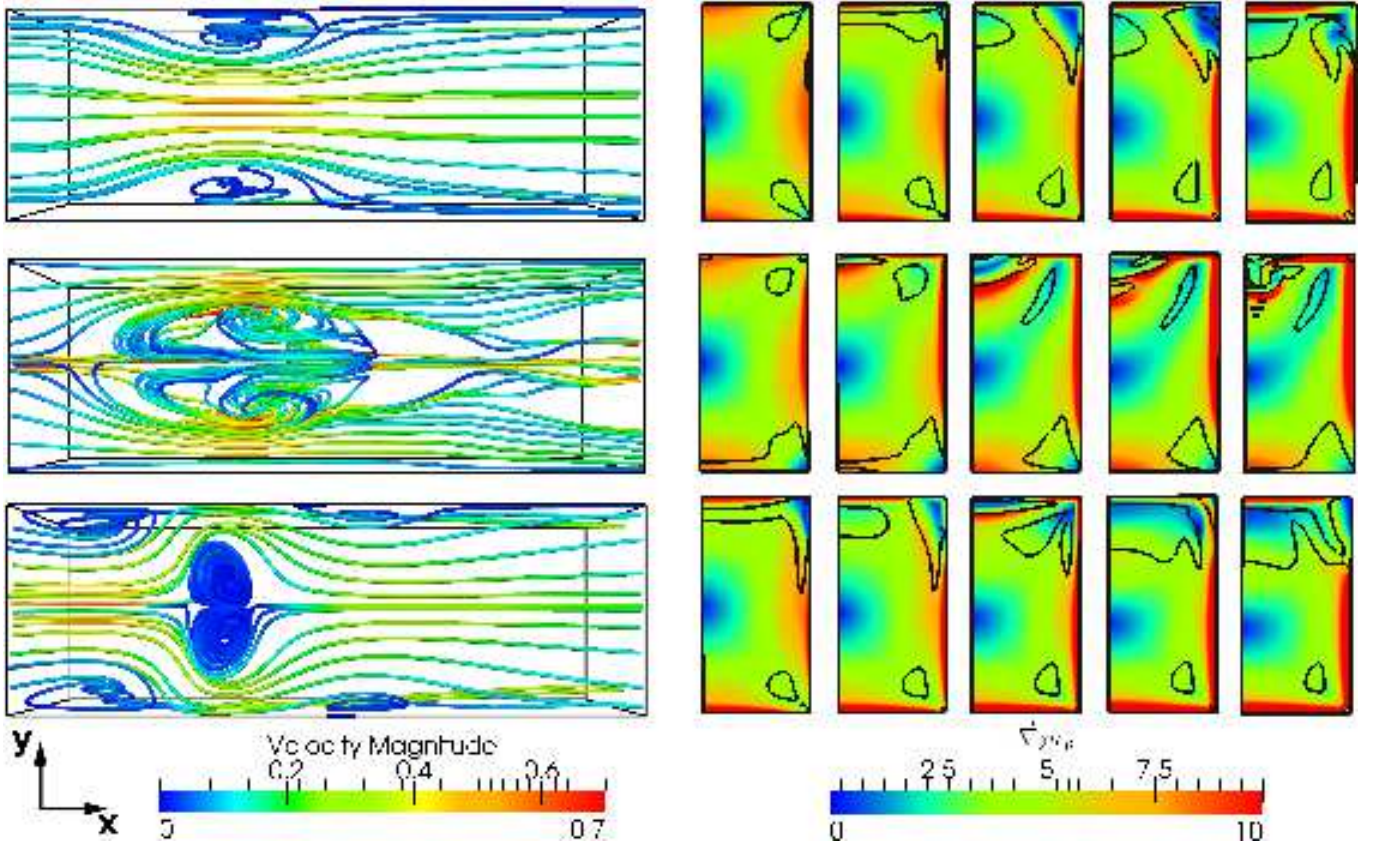


FIG. 13: Streamlines (left column) and inflection lines (right column) at $Re = 2000$, $Ha = 100$ and $h = 1.6$ for different orientations. Top row: wall-normal vertical dipole. Mid row: spanwise oriented dipole. Bottom row: streamwise oriented dipole. Streamlines are shown along top wall from $x = -2$ till $x = 5$. Color indicates the velocity magnitude. The panels to the right show the corresponding cross sections at streamwise positions $x = -2, -1, 0, 1$ and 2 . Due to symmetry only half plane is displayed. The background colors display the magnitude of the cross-stream gradient $\vec{\nabla}_2 u_x$. Black solid lines are the inflection lines as defined in Eq. (32).

the time-dependent behavior of the generated vortex structures, i. e., the vortex shedding, and the resulting structures in the wake.

The vortex shedding generates a turbulent wake which is displayed in Fig. 14. In parallel to several cross sections of the streamwise velocity along the duct, isocontours of $\lambda_2 = -1$ are shown where λ_2 is the second largest eigenvalue ($\lambda_1 \geq \lambda_2 \geq \lambda_3$) of the symmetric matrix

$$\Lambda_{ij} = S_{ik}S_{kj} + \Omega_{ik}\Omega_{kj} \quad (33)$$

which is composed of the rate of strain and vorticity tensors, respectively,

$$S_{ij} = \frac{1}{2} \left(\frac{\partial u_i}{\partial x_j} + \frac{\partial u_j}{\partial x_i} \right) \quad \text{and} \quad \Omega_{ij} = \frac{1}{2} \left(\frac{\partial u_i}{\partial x_j} - \frac{\partial u_j}{\partial x_i} \right). \quad (34)$$

Negative values, $\lambda_2 < 0$, denote vortex cores²⁷ which can be clearly identified as so-called hairpin structures in the figure. They are found close to the top wall in the beginning of the wake before the whole duct is filled with turbulent flow patterns further downstream.

Alternatively, the vortex shedding can be observed by the time signal of the Lorentz force itself. Both, the drag force component F_x and the lift force component F_z , show a periodic sinusoidal time dependence. The temporal modulation of the signal is weak compared to the absolute magnitude (cf. Fig. 18 below). For example, it is $F_x = -1.64 \cdot 10^{-1} \pm 4.67 \cdot 10^{-4}$ and $F_z = 1.74 \cdot 10^{-2} \pm 6.75 \cdot 10^{-4}$ for $Re = 2000$ and $Ha = 100$. Both forces oscillate with a frequency of $3.15 \cdot 10^{-1}$ inverse time units.

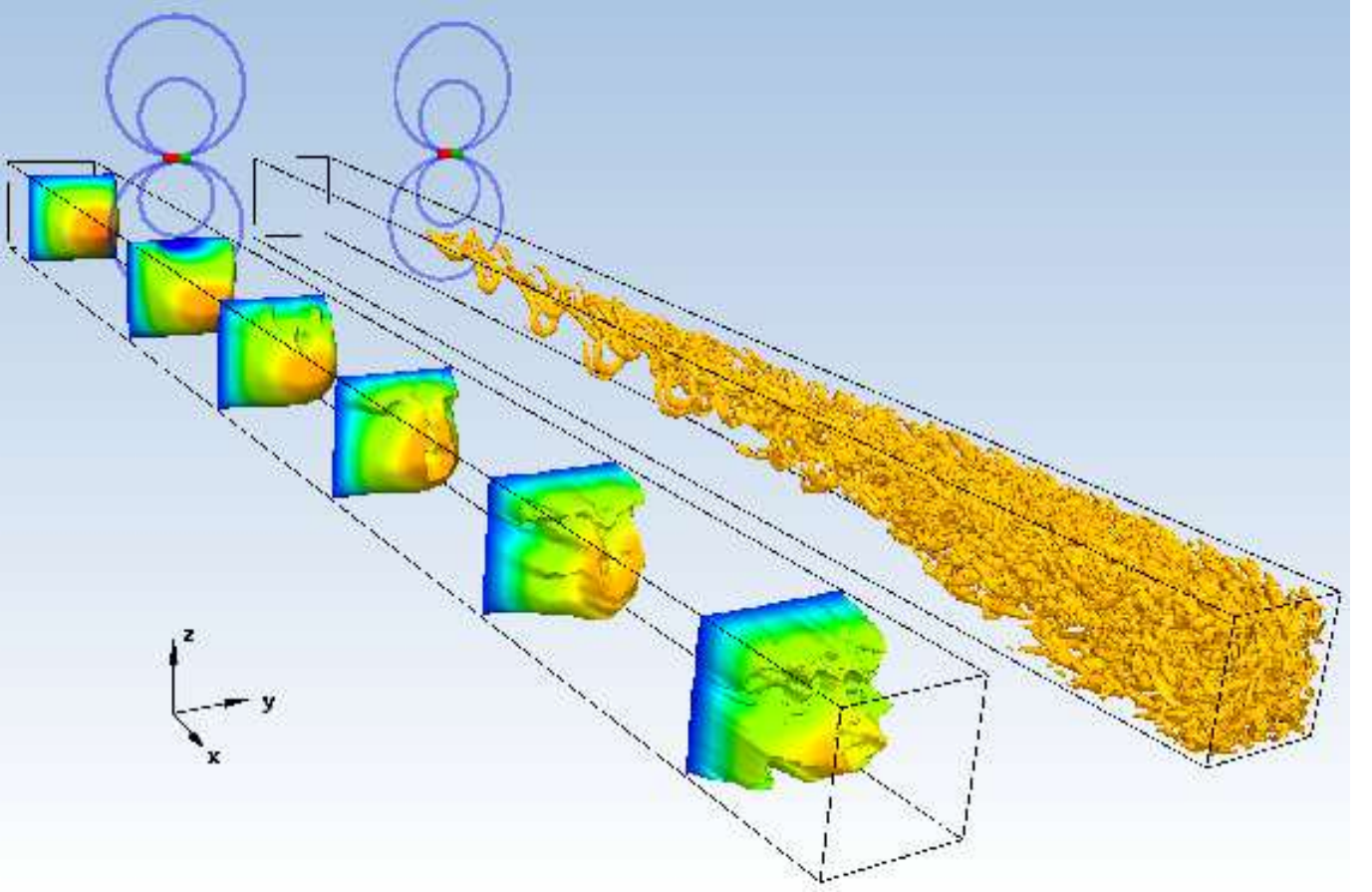


FIG. 14: Vortex shedding for a spanwise oriented dipole. Both ducts show the same snapshot for a Reynolds number $Re = 2000$, a Hartmann number $Ha = 100$ and a distance $h = 1.6$. The left duct displays instantaneous velocity profiles taken at 6 different streamwise locations between $x = -10$ and 40 . The right figure shows the isocontours of $\lambda_2 = -1$.

B. Reynolds number dependence at fixed Hartmann number

The time-dependent structures are shown in Fig. 15 for $Re = 2000$ in four snapshots in time intervals of approximately a quarter of the oscillation time. The figure displays the top view of the duct with the position of the dipole marked as a small black dot. The line of separation marks the region of locally reversed flow, i. e., points with $\partial_z u = 0$. Along this line the flow detaches from the surface. This criterion was also used by Mistrangelo (2011)³⁸ to determine the size of the vortex that occurs in a duct with sudden expansion in dependence on the applied homogeneous magnetic field. There, the magnetic field damps the vortex, in contrast to our investigation with the magnetic field being the source of the vortex formation.

In addition, Fig. 15 displays the structures in the wake. Here, the presented top surface is colored with $\partial_z u$. This gradient reaches its maximal value in the Hartmann layers. It should be noted here that the Hartmann layers and the vortex are not completely independent of each other. However, the mechanism that describes the interaction of both – and possibly drives the vortex shedding – has still to be determined.

To characterize the three-dimensional structure of the vortices, the λ_2 -criterion is used. The pictures on the right-hand side of Fig. 15 show the isocontours of $\lambda_2 = -0.5$. Each period a hairpin vortex structure is produced. It starts at time $t = 0$ with a small vortex that rotates clockwise about y , i. e., $(\nabla \times \vec{u})_y > 0$. This vortex is then advected further and surrounded by reversed flow until it passes the position of the dipole at $x = 0$ at time $t = 1/4 T$, T being the oscillation time. The vortex causes an increase of the width of the area of reversed flow as the back flow has to circumvent the vortex. In parallel, close to the corners of the duct, the Hartmann layer accelerates the flow. The accelerated fluid is blocked by the increase of the width of the reversed flow. This creates two extensions to the vortex at the sides, that are placed at $x = 0$ at time $t = 1/2 T$. The vortex is then pushed into the bulk away from the top surface (time $t = 3/4 T$). In this way, the backflow can move freely and recover the high magnitude at the beginning

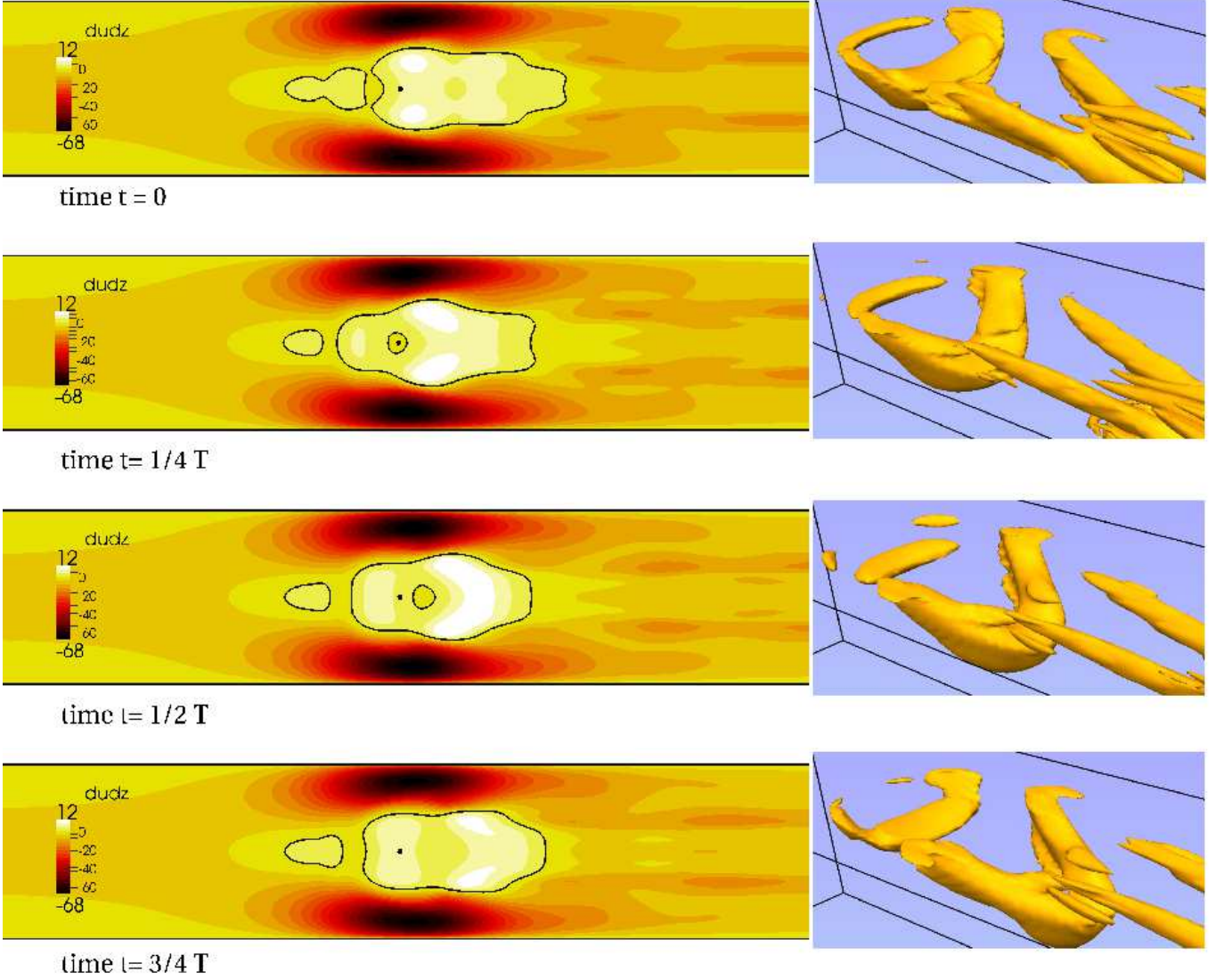


FIG. 15: (colour online) Visualization of the time-dependent structures for $Re = 2000$, $Ha = 100$, $h = 1.6$ and spanwise magnetic moment. Four snapshots are shown every 0.8 convective time units which cover one oscillation time of 3.168 time units. Left: Top surface with velocity gradient $\partial_z u$. Position of the dipole is indicated with a black dot. The black solid line indicates the line of separation $\partial_z u = 0$. Right: isocontours of $\lambda_2 = -0.5$ at same time. Direction of view in the picture is the same as in Fig. 17 b.

of the area of reversed flow. A next vortex is formed at time $t = T$ and the process repeats. A simple interpretation of this dynamics might therefore be that vortices are produced periodically by roll-up of a shear layer (Kelvin-Helmholtz instability) at the edge of the roughly hemispherical zone shielded by the dipole field from the main flow.

The vortices are transported into the wake and are stretched due to inertia and the shear at the top wall. Thereby, their shape forms into a hairpins like structure¹⁵. After the hairpin is moved into the wake a new vortex is created by the Lorentz force. Hairpins are well known to appear in vortical shear layers at walls²⁸ and occur in the transition to turbulence in the boundary layer. The spacial development of the wake is determined with the help of the momentum balance (14) in Fig. 16. This figure displays the terms time averaged over one period T , i.e., it shows the mean of 3168 snapshots at intervals of 0.001 time units, for $Re = 2000$ and $Ha = 100$. The well pronounced area of distortion with high Lorentz forces in the interval $-5 < x < 5$ is followed by the region of vortex shedding $5 < x < 20$. In this region, the flow is periodic in time with the same frequency as in the area of distortion. Here, the time averaged momentum balance resembles the laminar flow as the pressure balances the wall stresses and the contribution of the Lorentz force as well as of the momentum flux term are negligibly small. For $x > 25$ this changes to a transitional

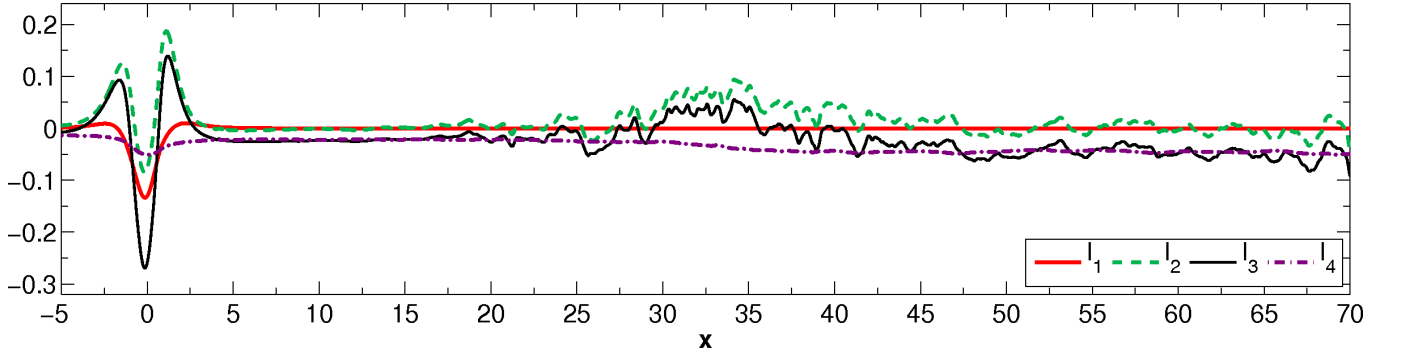


FIG. 16: (colour online) Streamwise variation of the different terms of the cross section averaged momentum balance (14) at $Re = 2000$, $Ha = 100$, $h = 1.6$ for spanwise orientation of the dipole. The data are time-averaged over one period as in Fig. 12 b. The four terms I_1 to I_4 are given again by Eqns. (15) to (18)

flow, where the momentum flux term dominates and the wall stresses increase up to a higher constant value as known from turbulent flow. In the beginning of the transitional range, the velocity profiles are found to resemble a turbulent flow but possess a symmetry plane $y = 0$. In this region, large scale vortices fill the whole cross section that break up further downstream. Our time averaging over one period does not converge in this range because the time-dependence of the structures is non-periodic. Although the computational domain and the calculation time are too short to obtain statistically converged values for the wake, one may expect a fully turbulent flow after a certain transition length. The calculation for $Re = 3000$ indicates that this length decreases for increasing Reynolds number.

In the following, we restrict the study of Reynolds number influence to three exemplary Reynolds numbers: $Re = 1000, 2000$ and 3000 are examined for fixed Hartmann number of $Ha = 100$. The streamlines for the three cases are shown in Fig. 17. The duct flow is stationary for $Re = 1000$, the wake remains laminar. As for $Re = 2000$, the wake undergoes a transition to turbulence for $Re = 3000$. The vortex structure below the dipole position remains similar for all three cases. The λ_2 -criterion reveals here the differences (cf. top row of Fig. 17). For $Re = 1000$ only one vortex is pronounced. In case of $Re \geq 2000$, additional vortices are produced in front of the dipole position, at $x < 0$, and during the vortex shedding. The amount and the strength of these vortical structures is enhanced at $Re = 3000$. The principal mechanism of the vortex shedding remains as explained above. The higher the Reynolds number the shorter are the generated hairpin structures in the wake. Besides the differences in the shape of the flow, the oscillation time is longer with increasing Re . For $Re = 2000$ an oscillation time of 3.168 was calculated, while for $Re = 3000$ it is 3.636 nondimensional time units. The time signal for both cases is depicted in Fig. 18.

We conclude from this section that the vortex shedding is a complex mechanism initiated by the Lorentz force. The Reynolds number determines how likely it is that the flow forms vortical structures and transforms into a turbulent flow in the wake. As a final step to this parameter study, it remains to investigate the influence of the Hartmann number on the created vortex.

C. Hartmann number dependence

To investigate the influence of the Hartmann number, we consider Reynolds number of 2000 and vary the Hartmann number between 25 and 130. For very small Hartmann number, there is almost no deformation of the flow visible. Fig. 19 shows examples of the streamlines for several Hartmann numbers. For $Ha = 25$, one may already observe the local Hartmann layers, but the Lorentz force is not strong enough to create a flow reversal. Such reversed flow is indicated by the streamlines from $Ha = 50$ and higher. A turbulent wake is observed for $Ha \geq 80$.

The dependence of the Lorentz force on the Hartmann number is summarized in Fig. 20. Here, the mean values of the forces are displayed with points and the range of the variation due to the vortex shedding is marked with two bars. Similar to the investigations in Sec. III, one finds the same power laws for the total forces, i.e., $F_x \sim Ha^2$ and $F_z \sim Ha^4$. The vortex shedding does not influence the power law as the oscillations of F_x and F_z are of the order of 1% and 10% of the forces, respectively.

As an additional characteristic the frequency of the vortex shedding can be obtained from the time signal of the force. Regarding the dipole as a magnetic obstacle allows one to compare the frequency of vortex shedding with typical values for flows generated past a solid cylinder (see e.g. Cuevas et al (2006)¹²). The nondimensional parameter for

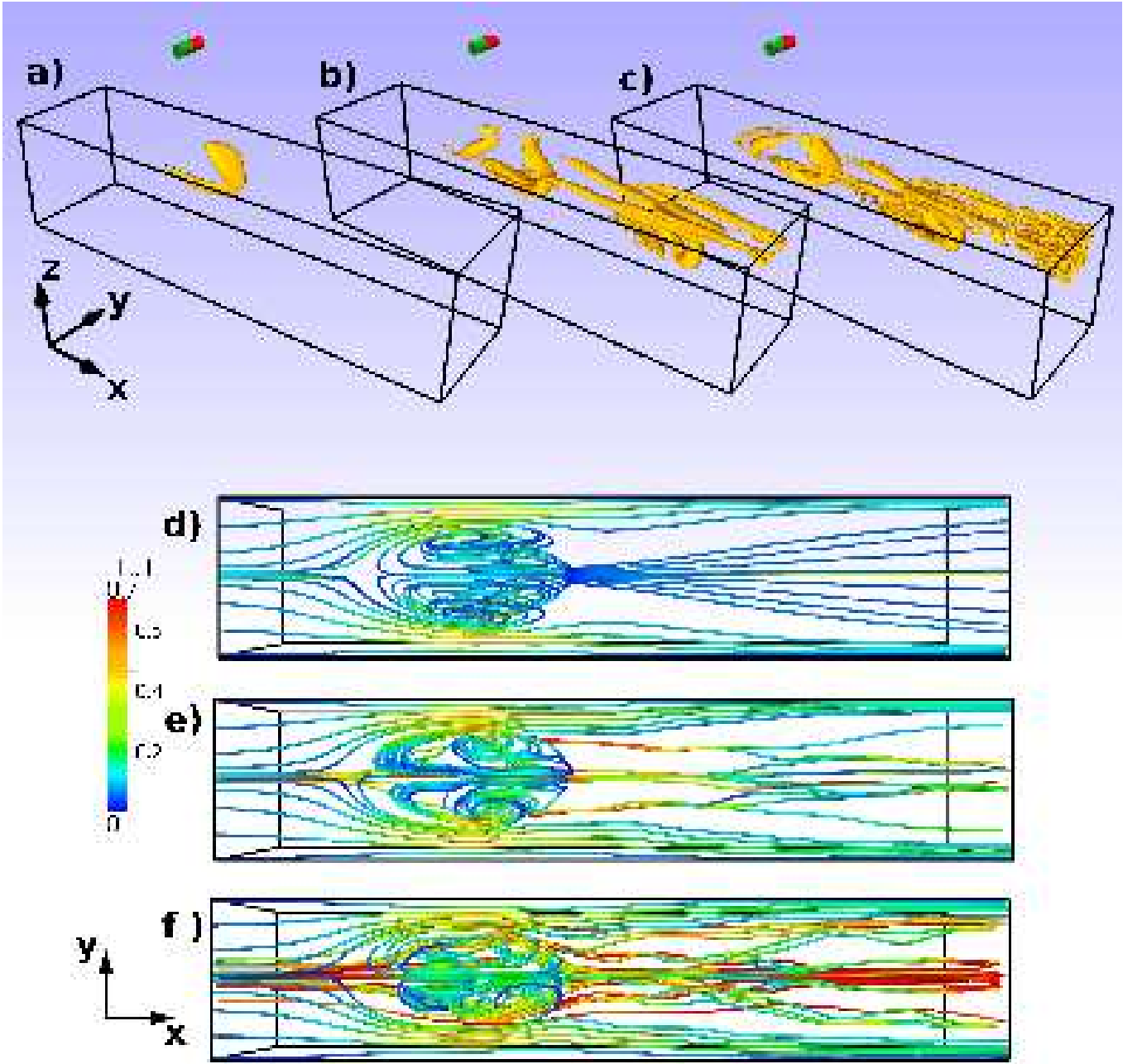


FIG. 17: (colour online) Influence of a spanwise oriented dipole on the flow for $Ha = 100$ and $h = 1.6$ at different Reynolds numbers: (a,d) is for $Re = 1000$, (b,e) for $Re = 2000$ and (c,f) for $Re = 3000$. Snapshots of isocontours of $\lambda_2 = -0.5$ in the range from $x = -3$ to $x = 5$ (a,b,c) and snapshots of streamlines for $x = -3$ to $x = 7$ (d,e,f)

such comparison would be then the Strouhal number

$$St = \frac{fD}{\bar{u}}. \quad (35)$$

Here, f denotes the frequency, \bar{u} the mean velocity and D the characteristic length of the obstacle, e.g. the radius of the cylinder. Whereas the frequency and the velocity are known in our setting, it is not obvious how to determine the characteristic length D of the magnetic obstacle. A good estimate for the size of the magnetic obstacle is the area in which the flow is detached from the wall, that was already discussed above (cf. Fig. 15). This region is stretched along

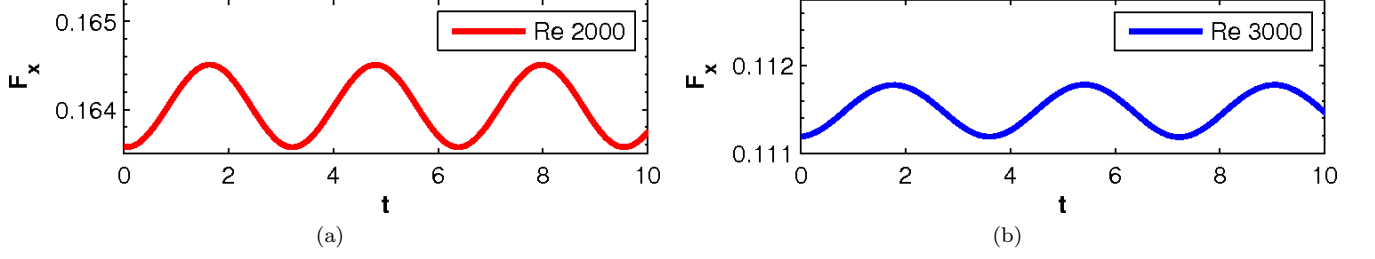


FIG. 18: (colour online) Time-dependent behavior of the force: Sinusoidal time signal for (a) $Re = 2000$ and (b) $Re = 3000$ with $Ha = 100$ and spanwise dipole in a distance of $h = 1.6$.

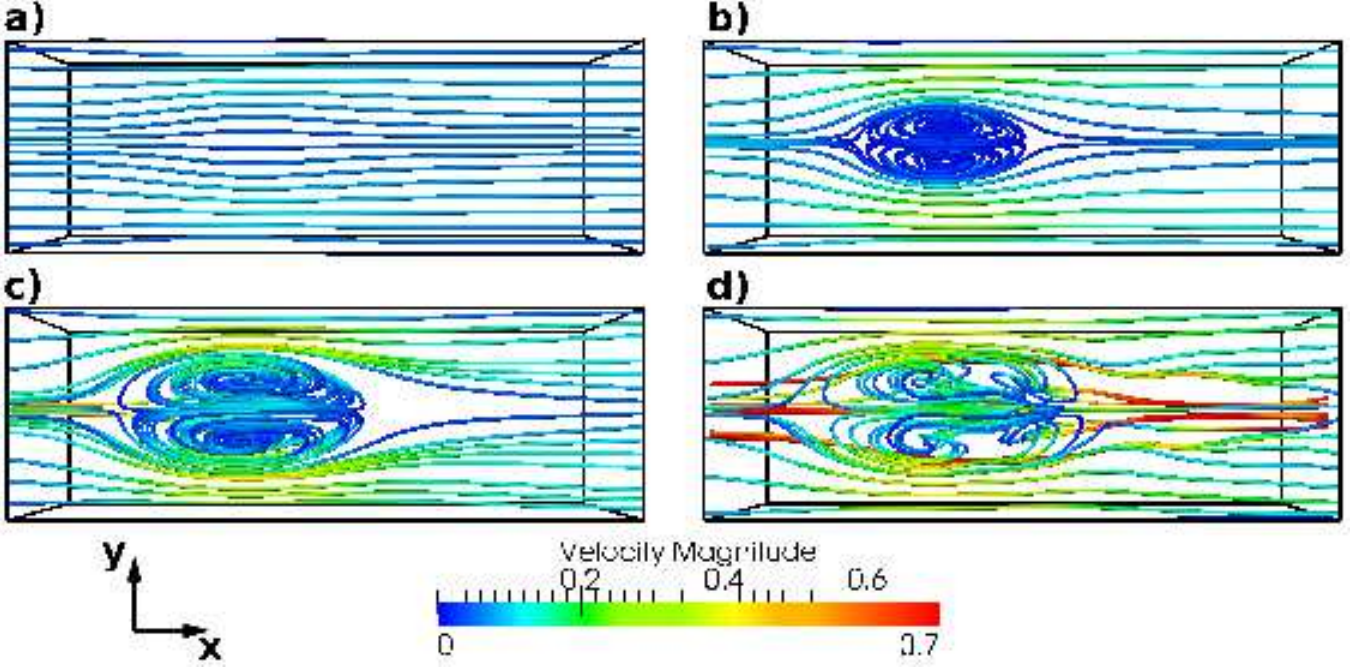


FIG. 19: (colour online) Streamlines for different Hartmann numbers and a spanwise dipole orientation at $Re = 2000$, $h = 1.6$. (a) $Ha = 25$, (b) $Ha = 50$ (c) $Ha = 70$ (d) $Ha = 80$. Box indicates the duct from $x = -2$ to $x = 5$. Total length was 15π .

the streamwise direction and the shape may change in time due to the vortex shedding. We define the characteristic length D of the magnetic obstacle as the maximal spanwise width of the area that is enclosed by $\partial_z u_x = 0$ at $z = 1$.

The obtained widths increase with increasing Hartmann number as displayed in Fig. 21 (a). In addition, the width is decreased with increasing Reynolds number. It is worth to note the influence of the interaction parameter $N = Ha^2/Re$ in the following example. The width is approximately the same for the simulations at $Re = 2000$ with $Ha = 80$ and at $Re = 3000$ with $Ha = 100$. Both cases have similar interaction parameter of $N = 3.2$ and 3.3 , respectively. This estimate does not hold for the regime without vortex shedding.

Furthermore, the frequency is found to decrease with increasing Hartmann number. This behavior was also observed for the two-dimensional flow with a small magnetic obstacle¹². The Strouhal number in Cuevas et al. (2006)¹² was obtained with a characteristic length that was fixed by the size of the small magnet. Therefore, they describe a decrease of the Strouhal number for increasing Hartmann number with values around $St \sim 0.1$. In a similar parameter study, Kenjeres (2012)²⁹ finds for the same interaction parameters as in our study $St = 0.282$ which is calculated from power spectra at several positions close to the magnetic obstacle. In the present work, the width of the area of reversed flow is used as a characteristic length of the magnetic obstacle. The width D is therefore a dynamic parameter that depends on Ha . If the Hartmann number is enhanced, the resulting Strouhal number increases with a gentle slope and reaches a saturation around $St \sim 0.16$ (cf. Fig. 21 (b) for $Re = 2000$).

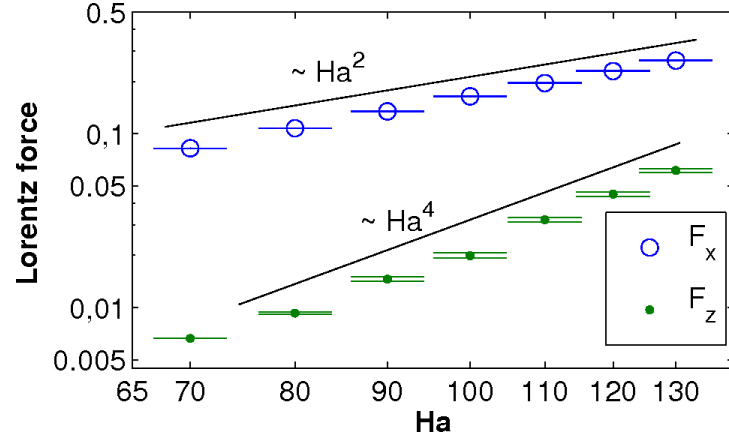


FIG. 20: (colour online) Lift and drag forces follow approximately the same power laws as in low Reynolds case (cf. Fig. 9). Points are given at the mean value while the vertical bars indicate the range of the variation of the time signal.

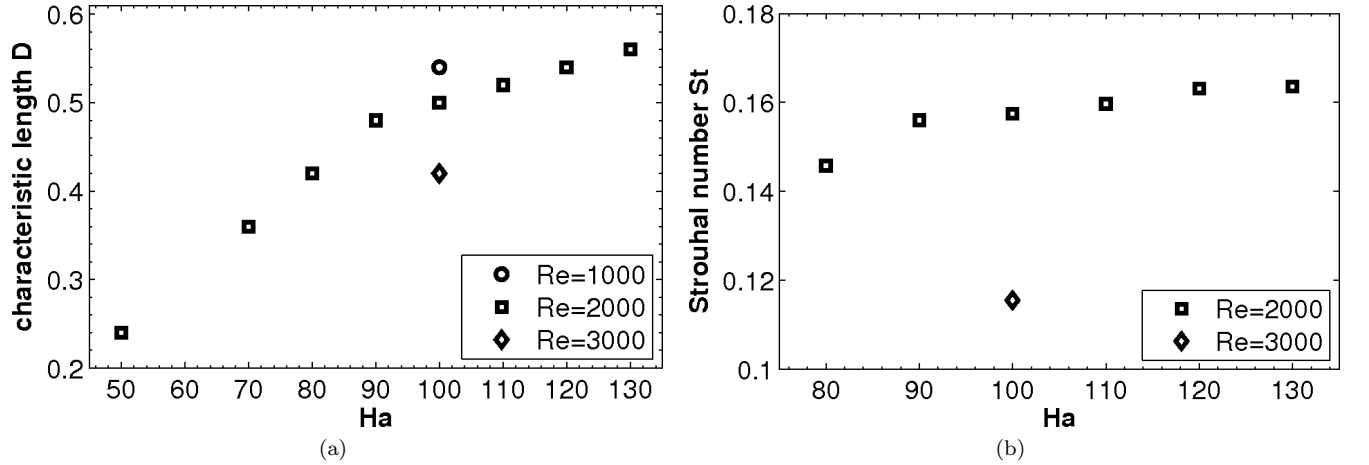


FIG. 21: Characteristics of the vortex shedding. (a) The width of the magnetic obstacle increases linearly for small Hartmann numbers and comes to a saturation for higher Ha , where the vortex shedding appears. Increasing the Reynolds number leads to decreased width. (b) The Strouhal number increases slightly with increasing Hartmann number and decreases with increasing Reynolds number.

The result can be compared to the flow around a solid cylinder. There, the Strouhal number is of the order $St \sim 0.2$ ⁶¹. Dousset and Potherat (2008)¹⁷ investigated the influence of a homogeneous magnetic field on the flow around a cylinder. In the regime of high Reynolds number, the Strouhal number was found to decrease with increasing Hartmann number. Thus, the homogeneous magnetic field damps the vortical structures. In our case, the inhomogeneous localized magnetic gives rise to the vortex formation and subsequent shedding.

Apart from the Strouhal number, it is desirable to have an additional quantity for the deflection of the flow that is caused by the dipole. The aim is therefore to characterize the structures in Fig. 19. A possible approach is to measure the vorticity, $\vec{\omega} = \nabla \times \vec{u}$, of the flow. For this, we consider the enstrophy over a duct fraction right below the dipole which is defined as

$$\Omega = \int_{[-1,1]^3} \frac{1}{2} |\nabla \times \vec{u}|^2 dV. \quad (36)$$

As the wake contains turbulent vortices, the integral is not applied to the whole domain. Thus, we focus on the area that is directly influenced by the dipole. Fig. 22 shows that the enstrophy increases linearly with the Hartmann number, which is caused by an increase of the vorticity $\vec{\omega} = \nabla \times \vec{u}$ in the vortex as well as the Hartmann layers. The strongest contribution comes from the partial derivative $\partial_z u_x$, which reaches maximal magnitudes in the Hartmann

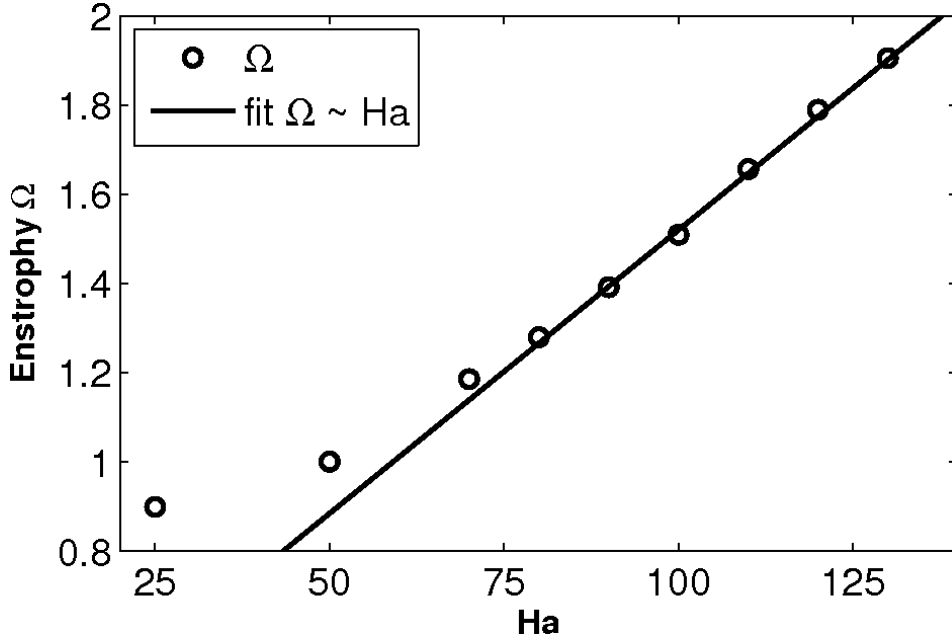


FIG. 22: The total enstrophy Ω as calculated in (36) is linear dependent on the Hartmann number. This behavior is originated in the local Hartmann layers. Data is given for $Re = 2000$, $h = 1.6$ and spanwise oriented dipole.

layer, as already mentioned above (cf. Fig. 15). An integration shows that the integral $\int_{[-1,1]^3} \frac{1}{2} |\partial_z u_x|^2 dV$ gives already about 80% of the magnitude of the total enstrophy Ω .

To explain the linear dependence on the Hartmann number, we recall the properties of the Hartmann layers in homogeneous magnetic fields. It is known from the analytic solution of the Hartmann channel flow⁴¹ that $u_x \sim 1 - \exp(-Ha z)$, where z measures the distance from the wall. We can therefore estimate $(\partial_z u_x)^2 \sim (Ha \exp(-Ha z))^2$ in the Hartmann layer. The width of the Hartmann layer is given by $\delta \sim 1/Ha$. Therefore, the integration of the enstrophy leads to $\Omega \sim \int_0^\delta |(\partial_z u_x)^2| dz \sim Ha$.

It has to be remarked here, that this explanation is only valid for the total enstrophy of duct flow in a uniform magnetic field when Ha is large. While the Hartmann layers show linear dependence of the total enstrophy on the Hartmann number, there are additional contributions from the Shercliff layers proportional to $Ha^{1/2}$. As a conclusion, the qualitative presentation of the flow structures in terms of the enstrophy (36) fails to provide details on the reversed flow and the vortex structures. Nevertheless, it gives a good criterion for the strength of the local Hartmann layers.

V. CONCLUSION AND OUTLOOK

In this work, we have investigated the influence of a localized inhomogeneous magnetic field on liquid metal flow in the quasi-static approximation. Our study focuses on the fundamental aspects of the structure formation. Therefore we use the simplest setting, a point dipole for the *localized* magnetic field and a simple shear flow in a square duct. It should therefore be considered as a paradigm for many realistic liquid metal flows. The magnetic field gives rise to a Lorentz force in the liquid that deforms the streamlines. Depending on the orientation of the dipole, areas of reversed flow and localized or local Hartmann layers are formed at the top surface due to strong Lorentz forces. The notion of local Hartmann layer is considered as a generalization of the canonical Hartmann flow and layer which arises due to the finite spanwise extension in the square cross section of the duct and the locality of the magnetic field. We have provided a systematic parameter dependence study which unraveled the local effects of the dipole field on the flow.

The parameter study is focused on the influence of the Reynolds and the Hartmann number. As expected the flow remains laminar and stationary for low Reynolds numbers. When the Reynolds number is increased, we observe that the length of the wake is increased. We showed that the spatial downstream decay rate of the deflected flow in the wake is proportional to $1/Re$. For $Re \geq 2000$, the spanwise oriented dipole in a distance of $h = 1.6$ triggers vortex shedding in case of Hartmann number above 80. The flow becomes time-dependent and eventually turbulent.

The Hartmann number affects the total Lorentz force. The drag component is proportional to Ha^2 , while the lift force behaves like Ha^4 for $Ha \leq 25$. The latter is connected with the nonlinearity in the Navier-Stokes equation. In

case of time-dependent flow with a spanwise oriented dipole, the vortex shedding leads to a sinusoidal force signal. The frequency of the signal corresponds to a Strouhal number that increases with increasing Hartmann number. The Strouhal number saturates around 0.16 which is comparable with classical flow past a cylinder. Nevertheless, it is not only the primary vortex, that has strong influence of the flow structure, but also the local Hartmann layers. Due to the formation of these boundary layers, the enstrophy of the deformed flow increases linearly with the Hartmann number.

Our study opens some new perspectives for flow manipulation and thus also for flow control. The described setting can be used to trigger turbulence in a laminar flow. This can be applied, e.g., for mixing injected substances or particles with the main flow. Such applications as well as experimental investigations of the problem have to be done with magnetic fields that are localized and inhomogeneous but not necessarily of the shape of a point dipole. Future numerical studies should include a turbulent inflow to model the experimental setting more realistically.

To obtain a complete understanding of the mechanism of the vortex shedding, the stability study can be extended. This could be provided by adding prescribed perturbations to a deformed but stationary flow. A more sophisticated way would be the direct optimal growth analysis as used by Barley et al. (2008)⁸ or a sensitivity study like Giannetti and Luchini (2007)²⁰.

Finally, the study should be extended to capture the influence of geometry parameters such as the distance of the dipole or its orientation. Here, the question arises whether the vortex shedding is still present if the dipole is oriented in an oblique orientation and what the optimal local Hartmann layers are to trigger flow transition. In addition, the symmetry of the given setting could be broken if the dipole is not positioned in the centerline of the duct, but with a certain offset. The influences of walls could also be studied by using rectangular ducts with non-square cross-section or pipes. These investigations open a huge parameter space that has to be considered in future works.

Acknowledgments

The authors wish to thank Dmitry Krasnov for providing the core of the used numerical code and for many fruitful discussions. We have also benefited from discussions with Oleg Zikanov, André Thess and Bernard Knaepen. The authors gratefully acknowledge the financial support from the Deutsche Forschungsgemeinschaft in the framework of the Research Training Group Lorentz Force Velocimetry and Lorentz Force Eddy Current Testing (grant DFG GK 1567/1). The numerical calculations have been performed on the cluster at TU Ilmenau and on the Juropa cluster at NIC/JSC (Jülich).

-
- ¹ J. C. Adams, P. Swarztrauber, and R. Weet. Efficient fortran subprograms for the solution of separable elliptic partial differential equations., 1999. <http://www.cisl.ucar.edu/css/software/fishpack/>.
 - ² C. Airiau and M. Castets. On the amplification of small disturbances in a channel flow with normal magnetic field. *Phys. Fluids*, 16(8):082991, 2004.
 - ³ T. Alboussière. Quasi characteristic MHD flows. *Comptes Rendus de l'Académie des Sciences-Series IIB-Mechanics*, 329(10):767, 2001.
 - ⁴ T. Alboussière, J. P. Garandet, and R. Moreau. Asymptotic analysis and symmetry in MHD convection. *Phys. Fluids*, 8(8):082215, 1996.
 - ⁵ T. Albrecht, R. Grundmann, G. Mutschke, and G. Gerbeth. On the stability of the boundary layer subject to a wall-parallel Lorentz force. *Phys. Fluids*, 18(9):098103, 2006.
 - ⁶ O. Andreev, Y. Kolesnikov, and A. Thess. Experimental study of liquid metal channel flow under the influence of a nonuniform magnetic field. *Phys. Fluids*, 18(6):065108, 2006.
 - ⁷ O. Andreev, Y. Kolesnikov, and A. Thess. Application of the ultrasonic velocity profile method to the mapping of liquid metal flows under the influence of a non-uniform magnetic field. *Exp. Fluids*, 46:77–83, 2009.
 - ⁸ D. Barkley, H. M. Blackburn, and S. J. Sherwin. Direct optimal growth analysis for timesteppers. *Int. J. Numer. Meth. Fl.*, 57:1435, 2008.
 - ⁹ D. Biskamp. *Nonlinear Magnetohydrodynamics*. Cambridge University Press, 1993.
 - ¹⁰ T. Boeck, D. Krasnov, and E. Zienicke. Numerical study of turbulent magnetohydrodynamic channel flow. *J. Fluid Mech.*, 572:179–188, 2007.
 - ¹¹ R. Chaudhary, S. P. Vanka, and B. G. Thomas. Direct numerical simulations of magnetic fields on turbulent flow in a square duct. *Phys. Fluids*, 22(7):075102, 2010.
 - ¹² S. Cuevas, S. Smolentsev, and M. A. Abdou. On the flow past a magnetic obstacle. *J. Fluid Mech.*, 553:227–252, 2006.
 - ¹³ S. Cuevas, S. Smolentsev, and M. A. Abdou. Vorticity generation in creeping flow past a magnetic obstacle. *Phys. Rev. E*, 74(5):1–10, 2006.
 - ¹⁴ P. A. Davidson. Magnetohydrodynamics in material processing. *Annu. Rev. Fluid Mech.*, 31:273–300, 1999.

- ¹⁵ P. A. Davidson. *Turbulence: An introduction for scientists and engineers*. Oxford University Press, 2004.
- ¹⁶ P. A. Davidson, editor. *An Introduction to Magnetohydrodynamics*. Cambridge University Press, Cambridge, UK, 2006.
- ¹⁷ V. Dousset and A. Pothérat. Numerical simulations of a cylinder wake under a strong axial magnetic field. *Phys. Fluids*, 20(1):017104, 2008.
- ¹⁸ S. Gavrilakis. Numerical simulation of low-Reynolds-number turbulent flow through a straight square duct. *J. Fluid Mech.*, 244:101–129, 1992.
- ¹⁹ D. Gerard-Varet. Amplification of small perturbations in a Hartmann layer. *Phys. Fluids*, 14(4):1458–1467, 2002.
- ²⁰ F. Giannetti and P. Luchini. Structural sensitivity of the instability of the cylinder wake. *J. Fluid Mech.*, 581:167–197, 2007.
- ²¹ J. Hartmann. Hg-dynamics I. Theory of the laminar flow of an electrically conductive liquid in a homogeneous magnetic field. *K. Dan. Vidensk. Selsk. Mat. Fys. Medd.*, 15(6):1–28, 1937.
- ²² J. Hartmann and F. Lazarus. Hg-dynamics II. Experimental investigations on the flow of mercury in a homogeneous magnetic field. *K. Dan. Vidensk. Selsk. Mat. Fys. Medd.*, 15(7):1–45, 1937.
- ²³ C. Heinicke. Spatially resolved measurements in a liquid metal flow with Lorentz force velocimetry. *Exp. Fluids*, 54(1560), 2013.
- ²⁴ C. Heinicke, S. Tynpel, G. Pulugundla, I. Rahneberg, T. Boeck, and A. Thess. Interaction of a small permanent magnet with a liquid metal duct flow. *J. Appl. Phys.*, 112(12):124914, 2012.
- ²⁵ A. Huser and S. Biringen. Direct numerical simulation of turbulent flow in a square duct. *J. Fluid Mech.*, 257:65–95, 1993.
- ²⁶ J. D. Jackson. *Classical Electrodynamics*. Wiley, New York, 3rd edition, 1998.
- ²⁷ J. Jeong and F. Hussain. On the identification of a vortex. *J. Fluid Mech.*, 285:69–94, 1995.
- ²⁸ J. Jeong, F. Hussain, W. Schoppa, and J. Kim. Coherent structures near the wall in a turbulent channel flow. *J. Fluid Mech.*, 332:185–214, 1997.
- ²⁹ S. Kenjeres. Energy spectra and turbulence generation in the wake of magnetic obstacle. *Phys. Fluids*, 24(11):115111, 2012.
- ³⁰ B. Knaepen and R. Moreau. Magnetohydrodynamic turbulence at low magnetic Reynolds number. *Annu. Rev. Fluid Mech.*, 40:25–45, 2008.
- ³¹ H. Kobayashi. Large Eddy Simulation of magnetohydrodynamic turbulent duct flows. *Phys. Fluids*, 20(1):015102, 2008.
- ³² D. Krasnov, O. Zikanov, and T. Boeck. Comparative study of finite difference approaches in simulation of magnetohydrodynamic turbulence at low magnetic Reynolds number. *Comput. Fluids*, 50(1):46–59, 2011.
- ³³ D. Krasnov, O. Zikanov, and T. Boeck. Numerical study of magnetohydrodynamic duct flow at high Reynolds and Hartmann numbers. *J. Fluid Mech.*, 704:421–446, 2012.
- ³⁴ D. Krasnov, O. Zikanov, M. Rossi, and T. Boeck. Optimal linear growth in magnetohydrodynamic duct flow. *J. Fluid Mech.*, 653:273–299, 2010.
- ³⁵ D. S. Krasnov, E. Zienicke, O. Zikanov, T. Boeck, and A. Thess. Numerical study of the instability of the Hartmann layer. *J. Fluid Mech.*, 504(2004):183–211, 2004.
- ³⁶ Dmitry Krasnov, André Thess, Thomas Boeck, Yurong Zhao, and Oleg Zikanov. Patterned turbulence in liquid metal flow: Computational reconstruction of the Hartmann experiment. *Phys. Rev. Lett.*, 110(8):084501, 2013.
- ³⁷ A. G. Kulikovskii. Slow steady flow of a conducting liquid at large Hartmann numbers. *Izv. Akad. Nauk SSSR, Mekhanika Zhidkosti i Gaza*, 3(2), 1968.
- ³⁸ C. Mistrangelo. Topological analysis of separation phenomena in liquid metal flow in sudden expansions. Part 2. Magnetohydrodynamic flow. *J. Fluid Mech.*, 674:132–162, 2011.
- ³⁹ R. J. Moreau. *Magnetohydrodynamics*. Kluwer Academic Publishers, 1990.
- ⁴⁰ Y. Morinishi, T. S. Lund, O. V. Vasilyev, and P. Moin. Fully conservative higher order finite difference scheme for incompressible flow. *J. Comp. Phys.*, 143(1):90–124, 1998.
- ⁴¹ U. Müller and L. Bühler. *Magnetohydrodynamics in Channels and Containers*. Springer-Verlag, 2001.
- ⁴² M.-J. Ni, R. Munipalli, N. B. Morley, P. Huang, and M. A. Abdou. A current density conservative scheme for incompressible MHD flows at low magnetic Reynolds number. Part I: On a rectangular collocated grid system. *J. Comp. Phys.*, 227:174–204, 2007.
- ⁴³ K. Niu. *Nuclear fusion*. Cambridge University Press, Cambridge, UK, 1989.
- ⁴⁴ J. Nordström, N. Nordin, and D. Henningson. The fringe region technique and the Fourier method used in the Direct Numerical Simulation of spatially evolving viscous flows. *SIAM J. Sci. Comput.*, 20(4):1365–1393, 1999.
- ⁴⁵ C. Pozrikidis, editor. *Introduction to Theoretical and Computational Fluid Dynamics*. Oxford University Press, 1997.
- ⁴⁶ J. Priede, D. Buchenau, and G. Gerbeth. Single-magnet rotary flowmeter for liquid metals. *J. Appl. Phys.*, 110(3), 2011.
- ⁴⁷ G. Rüdiger and R. Hollerbach. *The Magnetic Universe: Geophysical and Astrophysical Dynamo Theory*. Wiley-VCH Verlag GmbH & Co. KGaA, 2004.
- ⁴⁸ V. Shatrov and G. Gerbeth. Marginal turbulent magnetohydrodynamic flow in a square duct. *Phys. Fluids*, 8(5):084101, 2010.
- ⁴⁹ J. A. Shercliff, editor. *The Theory of Electromagnetic Flow Measurement*. Cambridge University Press, 1962.
- ⁵⁰ J. A. Shercliff, editor. *A Textbook of Magnetohydrodynamics*. Pergamon Press, 1965.
- ⁵¹ M. P. Simens, J. Jiménez, S. Hoyas, and Y. Mizuno. A high-resolution code for turbulent boundary layers. *J. Comp. Phys.*, 228:4218–4231, 2009.
- ⁵² F. Stefani, T. Gundrum, and G. Gerbeth. Contactless inductive flow tomography. *Phys. Rev. E*, 70(5):056306, 2004.
- ⁵³ A. Thess, E. Votyakov, B. Knaepen, and O. Zikanov. Theory of the Lorentz force flowmeter. *New J. Phys.*, 9(8):299, 2007.
- ⁵⁴ A. Thess, E. Votyakov, and Y. Kolesnikov. Lorentz force velocimetry. *Phys. Rev. Lett.*, 96(16):164501, 2006.
- ⁵⁵ S. Tynpel. *Magnetohydrodynamic duct flow in the presence of a magnetic dipole*. PhD thesis, University of Technology Ilmenau, Germany, 2013. <http://www.db-thueringen.de/servlets/DocumentServlet?id=22327>.

- ⁵⁶ S. Tynpel, D. Krasnov, T. Boeck, and J. Schumacher. Distortion of liquid metal flow in a square duct due to the influence of a magnetic point dipole. *Proc. Appl. Math. Mech.*, 12(1):567–568, 2012.
- ⁵⁷ M. Uhlmann and M. Nagata. Linear stability of flow in an internally heated rectangular duct. *J. Fluid Mech.*, 551:387–404, 2006.
- ⁵⁸ S. Vantieghem, X. Albets-Chico, and B. Knaepen. The velocity profile of laminar MHD flows in circular conducting pipes. *Theor. Comp. Fluid Dyn.*, 23(6):525–533, 2009.
- ⁵⁹ E. Votyakov, Y. Kolesnikov, O. Andreev, E. Zienicke, and A. Thess. Structure of the wake of a magnetic obstacle. *Phys. Rev. Lett.*, 98(14):144504, 2007.
- ⁶⁰ E. Votyakov, E. Zienicke, and Y. Kolesnikov. Constrained flow around a magnetic obstacle. *J. Fluid Mech.*, 610:131–156, 2008.
- ⁶¹ C. K. H. Williamson. Vortex dynamics in the cylinder wake. *Annu. Rev. Fluid Mech.*, 28:477–539, 1996.
- ⁶² Y. Zhao and O. Zikanov. Instabilities and turbulence in magnetohydrodynamic flow in a toroidal duct prior to transition in Hartmann layers. *J. Fluid Mech.*, 692:288–316, 2012.